Light Water Reactor Sustainability Research and Development

Mechanical and Microstructural Characteristics of Cast Stainless Steels after Thermal Aging for 10000 Hours

Cast Stainless Steel Aging (LW-17OR040215)

August 2017

U.S. Depart of Energy

Office of Nuclear Energy

DISCLAIMER

Mechanical and Microstructural Characteristics of Cast Stainless Steels after Thermal Aging for 10000 Hours

Thak Sang Byun (PI), Timothy G. Lach, David A. Collins, Emily L. Barkley

Pacific Northwest National Laboratory

Feng Yu

Electric Power Research Institute

TABLE OF CONTENT

LIST OF TABLES AND FIGURES

Mechanical and Microstructural Characteristics of Cast Stainless Steels after Thermal Aging for 10000 Hours

T.S. Byun, T.G. Lach, D.A. Collins, E.L. Barkley
Nuclear Sciences Division, Pacific Northwest National Laboratory, Richland, WA 99352

EXECUTIVE SUMMARY

The research on cast austenitic stainless steel (CASS) aging aims (i) to achieve scientific understanding on the aging and failure phenomena in CASSs using holistic experimental and modeling means and (ii) to provide practical and science-based model to predict the degree of thermal degradation of CASS components. The test materials in the project include four model CASSs (CF3, CF3M, CF8, and CF8M) and four EPRI-provided CASSs (CF3, two CF8s, and CF8M), which contain 4–33% δ-ferrite content. These materials have been thermally aged at two light water reactor (LWR)-relevant temperatures (290 and 330°C) and at two accelerated-aging temperatures (360 and 400°C) for more than two years as of today. This report is to present the results of experimental investigations for the model and EPRI-provided CASS materials after thermal aging up to 10000 hours. The main findings are summarized as follows:

The strength of the model CASSs with 4–16% initial δ-ferrite content decreased gradually with aging time and a faster decrease occurred at the relatively lower aging temperatures of 290 and 330°C. The thermal aging treatments had negligible effect on the general temperature dependence of strength in the model alloys. The yield and ultimate tensile strengths (YS and UTS) of the Mo-containing (2.3–2.6 wt.%) alloys, CF3M and CF8M, were always higher than those of their counterparts with lower Mo content (<0.5 wt.%), CF3 and CF8. The model alloys showed reduction of ductility during the short-term (1.5 kh) aging but experienced ductilization after 10 kh aging. The less ductile CF3 and CF3M alloys can still retain high uniform ductility more than ~20% over the whole test temperature range. The molybdenum containing alloys, CF3M and CF8M, showed evident aging temperature dependence in the decrease of upper shelf energy (USE); while the decrease of USE in CF3 and CF8 was rather sudden after aging for 1.5 kh, and then showed little aging temperature dependence in aging up to 10 kh. The ductile-brittle transition temperature (DBTT) data exhibited more aging-temperature and alloying element (Mo and C) dependences and a complex degradation behavior. The CF3M alloy showed its DBTT shifted above room temperature (+9°C or ΔDBTT = +135°C) after aging at 360°C for 10 kh. The smallest shift (ΔDBTT), +17, was found in the CF8 alloy after aging at 400°C for 10 kh. An aging recovery of DBTT (or negative shift of DBTT) between 1.5 kh and 10 kh was evident in the low temperature (290 and 330 °C) aging.

In the EPRI-provided CASSs with relatively high (11–33%) initial δ-ferrite content, the thermal aging effect was largely muted in strength parameters. The yield strength (YS) of the centrifugal cast alloys (from CF3-piping and CF8M-piping) was lower than those of the static cast alloys (from CF8-piping and CF8-elbow), which is mainly because the δ-ferrite content is higher in the static cast alloys (in the order of 30% versus of 10%). Despite the varied amounts of δ-ferrite, however, the UTS data show little difference between the centrifugal and static cast alloys. These high-ferrite CASSs, in general, only slightly lose their ductility during the 10 kh aging although the biggest and exceptional ductility reduction was observed in the static cast CF8-elbow material with the highest δ-ferrite content of 33%. It was found that the Mo content

can cause the biggest effect on USE before aging but the δ-ferrite content is the biggest factor determining the reduction of USE. The centrifugal cast CF3 (from Z21 pipe ring) showed significant DBTT shifts by aging but thermal recovery became apparent after the 10 kh aging at 360 and 400°C. The CF8M alloy (K23, centrifugal cast) also demonstrated the recovery behavior in the 400°C aging after its DBTT increased well above room temperature by 360°C aging. The static cast CF8 alloys have much higher δ-ferrite content of 25–33% in average and display correspondingly more significant degradation. Both of the static cast materials, CF8-ring and CF8-elbow, displayed profound and temperature-dependent shift of DBTT after aging.

Although the complexity and intersecting nature of microstructural changes makes it difficult to absolutely determine their effects on mechanical properties, some aspects could be confirmed through comprehensive microscopy analyses. A larger volume fraction of δ-ferrite in the sample, which is affected by the chemistry including the Mo and C concentrations and processing route that determines cooling rate, increases the potential for embrittlement as the ferrite phase and ferrite/austenite phase boundary undergo microstructural changes while the austenite matrix undergoes very limited changes. This study has shown that increasing Mo strongly increases the degree of spinodal decomposition with decreasing C slightly acting as a synergistic effect; and similarly, decreasing C has a strong tendency to increase the degree of G-phase precipitation with increasing Mo acting in a synergistic manner. The correlation between degradation of absorbed impact energy from the Charpy tests with the degree of spinodal decomposition and G-phase precipitation is rather strong; the CF8 alloy had the least amount of decomposition and G-phase precipitation and had the least change in impact properties, while the high Mo and low C alloys had the greatest degree of microstructural evolution and the largest reduction in impact properties. Also, Mo and C tend to segregate to the phase boundaries and enhance diffusion towards or away from the boundaries as well, due to the increased attraction/ repulsion induced by the Mo and C. These new phases and high solute concentration regions on the phase boundaries likely influence the thermal aging degradation of these materials. This can be inferred as the high Mo alloys, CF3M and CF8M, both have a larger aging temperature dependence on their impact properties.

1. INTRODUCTION

The cast austenitic stainless steel (CASS) materials are extensively used for many massive primary coolant system components of light water reactors (LWRs), including coolant piping, valve bodies, pump casings, and piping elbows. Many of these components are operated in complex and persistently damaging environments of elevated temperature, high pressure, corrosive environment, and in some instances radiation for long periods of time. Since a large number of CASS components are installed in every nuclear power plant and replacing such massive components is generally considered to be prohibitively expensive, any significant degradation in mechanical properties (cracking resistance, in particular) that affects the structural integrity of CASS components would raise a serious concern on the performance of entire nuclear power plant [1,2]. Therefore, the ongoing research, Cast Stainless Steel Aging, aims to expand scientific understanding on thermal-aging induced degradation in CASSs, and ultimately, to provide knowledge-based conclusive predictions for the integrity of CASS components during the service life extended up to and beyond 60 years [1].

The CASS materials for nuclear components are highly corrosion-resistant Fe-Cr-Ni alloys with 300 series stainless steel compositions and mostly austenite (γ)–ferrite (δ) duplex structures, which result from the casting processes consisting of alloy melting and pouring or injecting liquid metal into a static or spinning mold [3-6]. Although the commonly used static and centrifugal casting processes enable the fabrication of massive components with proper resistance to environmental attacks, the alloying and microstructural conditions are not highly controllable in actual fabrication, especially in the casting processes of massive components. The most common cast stainless alloy grades include the CF3 and CF8 alloy families with nominally ~19% Cr and ~10% Ni and 3–30% δ-ferrite [7-15]. In these corrosion-resistant Fe-Cr-Ni alloys, the minor phase (i.e., the δ-ferrite phase) is inevitably formed during the casting process, and is in a non-equilibrium state subject to detrimental changes during exposure to elevated temperature and/or radiation.

The degree of aging degradation in a CASS alloy depends on the chemistry and processing route of the alloy [7-13], because these determine the amount and distribution of δ-ferrite and small precipitates. The primary brittle fracture mechanism observed in a thermally embrittled duplex stainless steel is cleavage initiation at ferrite followed by propagation through separation of ferrite-austenite phase boundary. This cracking mechanism could be caused or enhanced by various microstructural changes during thermal aging, such as formation of a Cr–rich α'-phase through the spinodal decomposition of δ-ferrite, precipitation of G-phase and $M_{23}C_6$ carbide, and additional precipitation and growth of carbides and nitrides at ferrite-austenite phase boundaries [6-24]. In the austenite matrix, on the other hand, thermal aging induces various precipitations but usually causes a negligible to moderate effect on the properties of the phase [9-12].

This research project has investigated the thermal aging effects in four model CASSs (CF3, CF3M, CF8, and CF8M) and four EPRI-provided CASSs (CF3, two CF8s, and CF8M). These materials have been thermally aged at LWR-relevant temperatures (290 and 330°C) and at accelerated-aging temperatures (360 and 400°C). In the fiscal year, significant progresses have been made in characterization of the CASS materials after thermal aging up to 10 kh. This report is to present the experimental data from the characterization activities as well as to provide a detailed discussion on the correlation between microstructural and mechanical property changes in the model and EPRI-provided CASS materials.

2. EXPERIMENTAL

2.1. Chemical compositions of test materials

Since the volume fraction of δ-ferrite formed on casting is the most influential parameter in the degree and rate of aging degradation, eight different cast stainless steels were obtained for a wide range of δ-ferrite content. Investigating thermal aging effects with such different ferrite content is also needed to reflect the fact that a variety of cast stainless steels have been used in nuclear power plants as the reactor model and materials selection have evolved with the year of construction. The CASS alloys are typically graded by their chemistries and microstructural constituents [4-6]. The most common CASS materials used in nuclear power plants are the family of CF grades, which normally have key compositions of ~19% Cr and ~10% Ni and austenitic(γ)-ferritic(δ) duplex structures [6-9]. The main alloying elements in CASSs, i.e., Fe, Cr, Ni, Mn, Si and C, and the high-temperature cooling rate in casting process ultimately determine their resulting microstructural features including the volume fractions of ferrite (δ) and austenite (γ) phases.

Nuclear grade CASS alloys typically contain 3 to 30% δ-ferrite in austenite matrix [1]. Since the austenitic phase is highly stable in LWR temperature range, the amount of δ-ferrite phase is the most critical factor in the mechanical properties as well as in the aging process as higher aging degradation is usually associated with high ferrite content, in particular, with > ~15% δ-ferrite where a near complete contiguity of ferrite phase can be achieved. This is because the most common embrittlement mechanism in CASS materials occurs in the δ-ferrite phase (i.e., the spinodal decomposition of the δ-ferrite phase into α-ferrite and brittle ά-martensite) and both crack initiation and propagation involve these phases and their interfaces [7-13]. More ferrite content generally leads to a higher tensile strength due to its intrinsic strength and more precipitates while austenite phase usually has higher ductility and fewer precipitates.

The most common alloys in nuclear power plants include the CF3 and CF8 grades of alloys with the CF3, CF3A, CF3M, CF8, CF8A, and CF8M being the most prominent variants [5,7-14]: Typical nuclear power plants have been using CF8, CF8A, CF8M, and CPF3M for their reactor coolant and auxiliary system piping, pump cases, valve bodies, and fittings (note: A-anneal, M-molybdenum doped, and P-piping). In later construction applications and replacements, the CF3s with lower carbon content (< 0.03%) have been used rather than CF8s (C < 0.08%). This is because lower carbon content is favored for less δ-ferrite formation as well as for less carbide formation at boundaries and interfaces; however, other factors such as cooling rate (or component size) and Mo content can be more influential on the formation of δ-ferrite.

Tables 1 through 3 summarize the chemistries of the four model and four EPRI CASS alloys, along with the reference compositions in ASTM specification for these alloys [6]. The primary controlled-elements are C and Mo: the CF3 and CF3M has lower carbon content < 0.03 wt.% and CF3M and CF8M are alloyed with 2-3 wt.% Mo. The four model CASS alloys (i.e., CF3, CF3M, CF8, and CF8M) have been produced in the form of small (Ø~10 cm × L~40 cm) ingots to have relatively low δ-ferrite volume fractions (4-16%), while the four EPRI-provided alloys (i.e., CF8M(K23), CF8(S43), CF3(Z21), and CF8(ELB)) were taken from the simulated or vintage components in EPRI's storage yard in Charlotte, NC, for higher δ-ferrite content (11–33%). All chemical composition data were produced by Dirats Laboratories in Westfield, MA.

Table 1. Chemical compositions of model CASSs in wt.% or in ppm (for C, S, O and N)

Grade (Equivalent Wrought Steel)	Fe	Cr	Ni	Mn	Mo	Si	Cu	Co	V	P	C	S	O	N
CF3 (304L)	Bal.	19.17	8.11	1.44	0.34	0.99	0.41	0.18	0.07	0.029	262	324	204	1020
CF3M (316L)	Bal.	19.28	9.81	1.14	2.30	1.22	0.28	0.15	0.05	0.033	284	253	224	838
CF8 (304)	Bal.	18.72	8.91	1.10	0.29	1.27	0.29	0.15	0.05	0.026	665	376	161	606
CF8M (316)	Bal.	18.52	10.38	0.65	2.33	1.02	0.33	0.17	0.06	0.031	433	243	207	1020

Table 2. Chemical compositions of EPRI-provided CASSs in wt.% or in ppm (for C, S, O and N)

Grade (Component*)	Fe	Cr	Ni	Mn	Mo	Si	Cu	Co	V	P	C	S	O	N
CF8M (K23, 6.9 cm thick piping) Simulated/Centrifugal	Bal.	20.77	10.16	0.95	2.51	0.85	0.39	0.16	0.07	0.032	590	220	25	1500
CF8 (S43, 8.6 cm thick piping) Vintage/Static	Bal.	20.01	8.61	0.57	0.30	1.31	0.07	0.08	0.02	0.031	590	130	36	450
CF3 (Z21, 10.4 cm thick piping) Vintage/Centrifugal	Bal.	20.69	9.57	0.89	0.14	1.10	0.10	0.03	0.04	0.023	220	30	53	572
CF8 (ELB, 20.3 cm thick elbow) Vintage/Static(Elbow)	Bal.	21.20	8.45	0.61	0.18	1.78	0.16	0.04	0.02	0.017	360	60	53	411

Table 3. Chemical compositions of cast austenitic stainless steels in ASTM specification (in wt.% for major alloying elements or in ppm for C, S, O and N)

Grade	Fe	Cr	Ni	Mn	Mo	Si	P	C	S	N
CF3 (304L)	Bal.	17-21	8-12	<1.5		<1.5	<400	<300	<400	
CF3M (316L)	Bal.	17-22	9-13	<1.5	2-3	<1.5	<400	<300	<400	1000-2000
CF8 (304)	Bal.	18-21	8-11	<1.5		<2	<400	<800	<400	
CF8M (316)	Bal.	18-21	9-12	<1.5	2-3	<2	<400	<800	<400	

2.2. Content of δ-ferrite in duplex structures

Table 4 lists the ferrite content of the CASS alloys in the as-cast condition. The ferrite numbers (FNs) were measured from Charpy impact or three-point bend bar fracture specimens using a ferrometer (model: Feritscope-FMP30C of Fisher co.). For each alloy, many (30–50) FN data were measured and statistically treated for providing the data in the table. The volume fraction data listed were converted from the FN measurements.

Among the model alloys the CF3M alloy has the highest volume fraction average of 15.7%, which is followed by CF3 with 12.4%. The CF8 and CF8M contain relatively low δ-ferrite content, 4.7 and 5.6%, respectively. The chemical composition and cooling rate determine their microstructure after casting, in particular, determining the volume fractions of ferrite (δ) and austenite (γ) phases. The δ-ferrite content can vary widely with the thermal history of casting process since the cooling rate on passing the ferrite formation area in the phase diagram might determine the total exposure time for ferrite

formation. These model alloys were likely produced at rather high cooling rates as the ingots were only ~10 cm diameter.

Table 4 also shows that the centrifugal cast CF3 and CF8M pipings have similar δ-ferrite content as those of the model alloys CF3 and CF3M (< 16%). Both the static cast materials, CF8-piping and CF8-elbow, contain much higher δ-ferrite content of 25–33%. The CF8 (ELB) alloy has gained the highest δ-ferrite content (33%) as its cooling was the slowest due to the static casting of the thickest (~20 cm) component. In conclusion, the casting method is believed to be the biggest factor in determination of δ-ferrite content, which is followed by the Mo and C content.

Table 4. Content of δ-ferrite measured in as-cast condition (the volume fraction data (in %) were calculated from FN measurements)

Grade		FN	STDEV (FN)	Vol.%	STDEV (Vol.%)
CF3 (Model Alloys)		11.4	0.88	**12.4**	1.02
CF3M (Model Alloys)		14.6	1.53	**15.7**	1.76
CF8 (Model Alloys)		4.2	1.01	**4.7**	1.17
CF8M (Model Alloys)		4.9	0.52	**5.6**	0.60
CF8M Simulated/Centrifugal	K23	10.4	1.69	**11.4**	1.94
	K25*	11.8	1.82	**12.9**	2.09
CF8 Vintage/Static	S43	24.7	3.13	**25.1**	3.57
	S52*	31.1	3.35	**30.6**	3.82
CF3 Vintage/Centrifugal	Z21	10.8	2.21	**11.8**	2.53
	Z43*	11.3	2.60	**12.3**	2.97
CF8 (ELB) Vintage/Static (Elbow)		34.0	3.75	**33.0**	4.26

Only tensile test data in as-cast condition are included in this report.

2.3. Thermal aging history

The CASS materials have been thermally aged in large capacity furnaces set at 290, 330, 360, and 400°C since either year 2014 or 2015, along with the reference wrought stainless steels and weld alloys. The aging time for the materials, except for the weld alloys, have reached 20 kh in this fiscal year. Figure 1 summarizes the aging schedule for the whole materials portfolio of the project. The results presented in the report are those for the four model alloys aged for 0h, 1.5 kh and 10 kh and for the four EPRI-provided alloys after aging for 0h and 10 kh.

If using a typical activation energy of 250 kJ/mole in calculation of aging parameter, it can be assessed that the thermal aging at 400°C for 10 kh corresponds to more than 60 years of service in LWR core condition (325°C) and the 400°C aging for 1.5 kh is approximately equivalent to a 50 year service in LWR system. The aging treatments at other temperatures are supposed to produce under aged conditions when compared to the 60 year service in LWR.

Aging Period in Hour (Year)	FY 2014	FY 2015	FY 2016	FY 2017	FY 2018	FY 2019	TBD
Model Alloys	CF3, CF3M, CF8, CF8M (static)						
1500 (0.17)	▬▶						
10000 (1.14)		▬▬▬▬					
30000 (3.42)		▬▬▬▬▬▬▬					
>40000		▬▬▬▬▬▬▬▬▬▬▬▬▬▬▬					
EPRI Alloys	CF8M: K10(523 & 525 rings)-centrifugal, simulated (ID: K23, K25) CF3: Z12(21 & 43 rings)-centrifugal, vintage (ID: Z21, Z43) CF8: 3(-4043 & -14352 rings)-static, vintage (ID: S43, S52) CF8: Elbow block (ID: ELB)						
5000 (0.57)		▬▬▬					
10000 (1.14)		▬▬▬▬					
30000 (3.42)		▬▬▬▬▬▬▬					
>40000		▬▬▬▬▬▬▬▬▬▬▬▬▬▬▬					
Wrought SS	304L, 316L						
1500 (0.17)	▬▶						
10000 (1.14)		▬▬▬▬					
30000 (3.42)		▬▬▬▬▬▬▬					
>40000		▬▬▬▬▬▬▬▬▬▬▬▬▬▬▬					
KHNP Welds	308L, 316L, 347						
10000 (1.14)			▬▬▬▬				

Figure 1. Short- & long-term ageing schedules for the CASS alloys, wrought stainless steels, and stainless steel welds. The vertical dashed red line indicates the current time.

2.4. Mechanical testing and analysis

The uniaxial tensile testing and Charpy impact testing were performed for the aged and nonaged CASSs. The tensile specimens were SS-3 dog-bone shaped flat specimens with the gage section dimensions of 7.62 mm in length×0.76 mm in thickness×1.52 mm in width. The uniaxial tensile tests were carried out at room temperature (RT) to 400°C at a displacement rate of 0.5 mm/min, which corresponds to a nominal strain rate of 0.0011/sec. The engineering strength and ductility parameters were obtained from the raw tensile load-displacement and specimen dimension data and the results are presented in this report.

The impact tests were carried out in a 350 J capacity Charpy impact tester using the standard Charpy V-notched specimens (10 mm × 10 mm × 25 mm bars with a 2 mm deep 45° notch). A set of 10–12 tests were carried out for each materials condition in a wide temperature range to construct a temperature transition curve.

For each of the absorbed energy dataset, curve fitting analysis was performed to obtain the temperature transition parameters using a four parameter hyperbolic tangent function [28,29]:

$$E(T) = A + B \times \tanh\left(\frac{T-D}{C}\right) \qquad (eq.1)$$

where A is the vertical position of the inflection point, B is the vertical distance between point A and the upper and lower shelves, C is one-half the width of the transition region, and D is the horizontal position of the inflection point. As shown in Figure 1, key transition curve parameters can be defined using these parameters: the value $A+B$ is defined as the upper shelf energy (USE), and $A-B$ is defined as the lower shelf energy (LSE). The parameter D becomes the ductile-brittle

transition temperature (DBTT), which is the midpoint temperature in the temperature-transition region. The best fit curves can be found using the ordinary least squares (OLS) regression technique or similar regression methods. In practical analysis the two parameters, the LSE and USE, can be determined by plotting measured absorbed energy data, and therefore the DBTT value is used as an iteration parameter. In the cases that the absorbed energy (usually ≤ 20 J) doesn't reach the lower shelf within the test temperature range, the LSE can be set at 20 J for stainless steels [30,31].
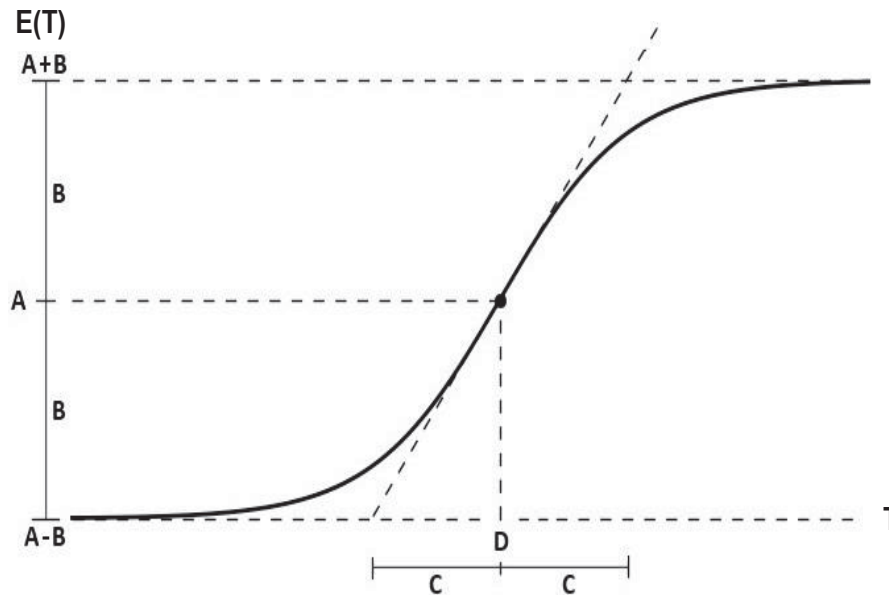
Figure 2. Definition of parameters in the ductile-brittle transition curve.

A drawback of using the symmetrical hyperbolic tangent function is that its application can be often limited to the transition region and its vicinity. The hyperbolic tangent function asymptotically approaches their shelf values as the test temperature decreases and increases in lower and upper shelf regions, respectively. In most of the ferritic and austenitic steels, however, the impact energy (or toughness) measurement decreases with test temperature after passing a maximum plateau. In the present analysis, the average of a few absorbed energies at the plateau around the maximum was used as the USE. Another drawback we can encounter when we use the traditional DBTT definition is that a dramatic reduction of USE can cause a net effect of moving DBTT lower and a negative shift of DBTT can be measured even if the test material has been degraded. Examples will be shown in a later section. A nil-ductility temperature (NDT) can be used to avoid this effect: the 41J (30 lb-ft) index temperature, T_{41J}, can be calculated from the same fitted function [31].

2.5. Microstructural characterization

Aberration-corrected TEM and STEM and atom probe tomography (APT) were the primary means of studying the changes the materials underwent when subjected to thermal aging using a probe aberration-corrected JEOL ARM200F TEM/ STEM. Bright field (BF) and high angle

annular dark field (HAADF) micrographs were obtained in STEM mode in conjunction with EDS for chemical analysis. BF and DF TEM micrographs, along with selected area electron diffraction (SAED) patterns, imaged the microstructural changes and diffraction contrast among different phases.

Cross-sectional areas were obtained using a dual beam focused ion beam/ scanning electron microscope (FIB/SEM) (FEI Helios NanoLab 660 or FEI Quanta) and conventional TEM lift-out methods to a thickness of about 500 nm at operating voltage of 30 kV on gold half-grids [32]. Further thinning was performed by a custom fabricated assembly to electrochemically polish the samples with 5% perchloric acid at -50 °C and 11 V. This was done to minimize gallium-ion damage that may appear similar to microstructural changes during thermal aging when observed in TEM/STEM.

Atom probe tomography (APT) was performed on a Cameca LEAP 4000X using voltage mode with a pulse fraction of 20% at 250 kHz at a temperature of 40 K. APT tips were sharpened using the FIB/SEM annular milling technique on 6×6 Si microtip arrays [33]. Ga-ion damage is minimized using low kV final sharpening. Reconstructions and analyses were performed using Cameca's IVAS 3.6.14 software.

3. EFFECTS OF THERMAL AGING ON STRENGTH AND DUCTILITY

3.1. Changes of YS and UTS in model alloys

The thermal aging effects on the engineering strength and ductility parameters of model CASS alloys (CF3, CF3M, CF8 and CF8M) are discussed in this section. It is worth nothing that the model CASS alloys contain relatively low content of δ-ferrite (4–16% in the as-cast condition) and hence they are expected to show relatively less significant and gradual property degradation on thermal aging. As will be discussed in the later section, on the other hand, the EPRI-provided CASS alloys contain similar or higher δ-ferrite content, and therefore some of them will display relatively higher thermal degradation. In those EPRI-provided alloys we can also expect to observe the effect of different casting processes (i.e., centrifugal and static casts) in the aging degradation behavior. In the model alloys, however, the chemical composition will be the only parameter that can affect the aging behavior as they have been produced in the same casting route and size.

Figures 3 and 4 compare, respectively, the yield strength (YS) and ultimate tensile strength (UTS) of thermally aged and nonaged model CASS alloys plotted against test temperature. Although these strength datasets display no significant aging-induced changes, there are a few aspects worth being discussed. First of all, the thermal aging treatment gradually reduced the strength of model alloys with aging time and the reduction was higher at the relatively lower aging temperatures, 290°C and 330°C. The thermal aging for 1.5 kh has caused an overall small change in strength, regardless of the differences in chemistry and aging temperature: both the YS and the UTS of CF3, CF8, and CF8M alloys were slightly lowered by the 1.5 kh aging [31], while the CF3M alloy retained its strength after the short aging treatment. The 10 kh aging induced further softening in all four model alloys. This softening during aging might result from a few softening mechanisms, such as dislocation annihilation, reduction in solid solution effect, and other stress relaxation effects, which may over-compensate the hardening amount by precipitation. The precipitates that can contribute to hardening may include the ά particles from

ferrite decomposition, G-phase formation, and carbide precipitation. It is also observed in all model alloys and in both strength parameters that the reduction of strength is highest at the lowest aging temperature of 290°C. This should indicate that the age softening effect is more dominating at lower aging temperature. In addition, the overall change in strength can also be measured by the band widths of the YS and UTS data for each alloy. Both the YS and UTS data after aging at different temperatures (290, 330, 360, and 400 °C) for 1.5 and 10 kh are contained within similar band widths over the whole test temperature range, 290–400°C. The band widths became almost doubled as the aging period increased from 1.5 kh to 10 kh, which also reflects continued softening on aging.

Second, it is commonly observed in Figure 3 and Figure 4 that the thermal aging up to 10 kh has not changed the temperature dependence of strength in the model alloys, which is that YS and UTS decrease with test temperature at similar rates but become nearly temperature-independent in the aging temperature range of 290–400°C. Such a little change in the temperature dependence may indicate that the strengthening mechanisms being operated in the test temperature range remain unchanged during thermal aging. This relatively aging-insensitive aspect in strength is contrary to the impact energy transition behavior to be described in the later sections.

Third, one aspect consistently observed in the strength data is the difference between alloys. The strengths of the Mo-containing (2.3–2.6 wt.%) alloys, CF3M and CF8M, are always higher than those of their counterparts with lower Mo content (< 0.5 wt.%), i.e., CF3 and CF8. It seems that the difference between these two alloy groups remains approximately unchanged after the thermal aging treatments.
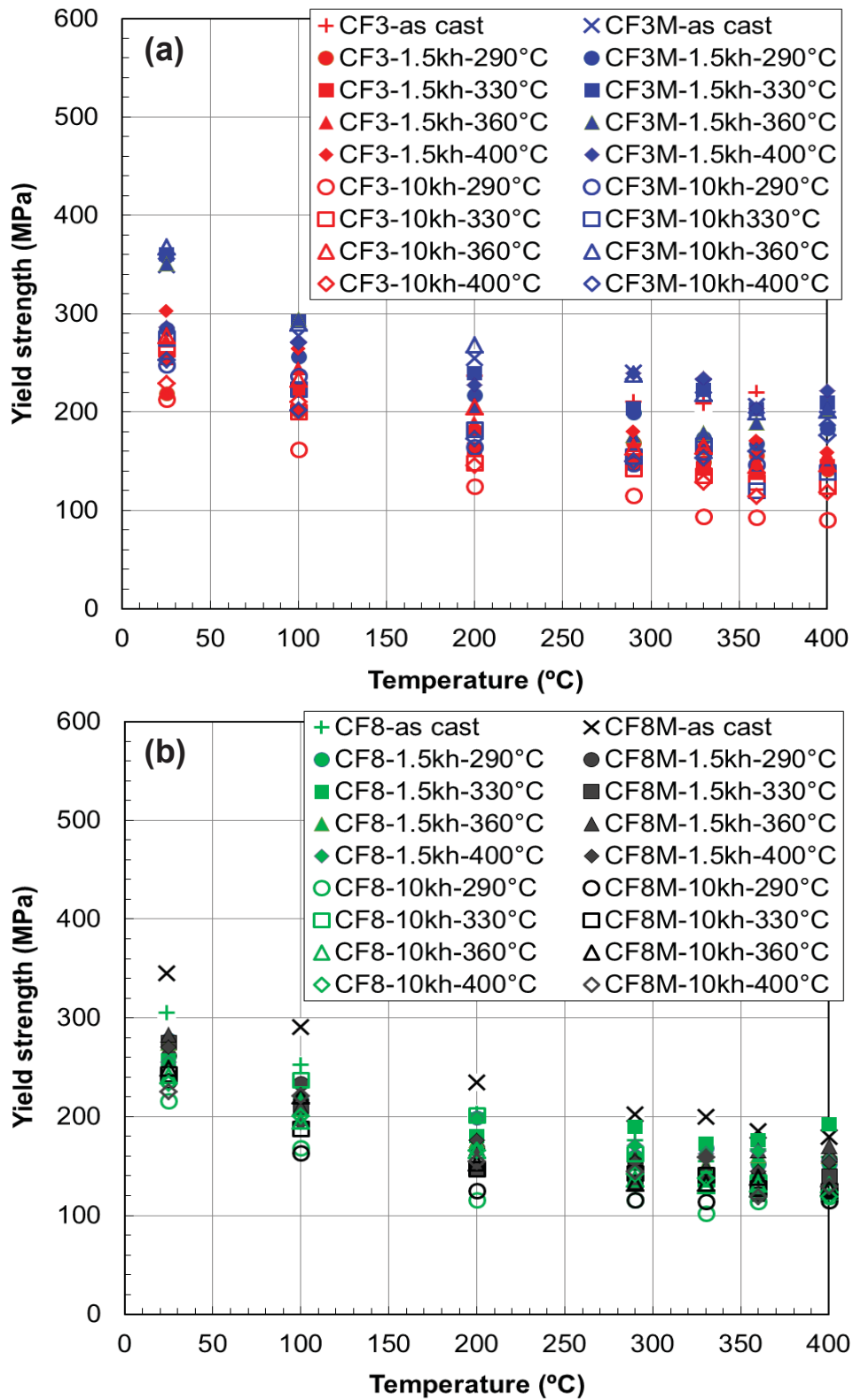
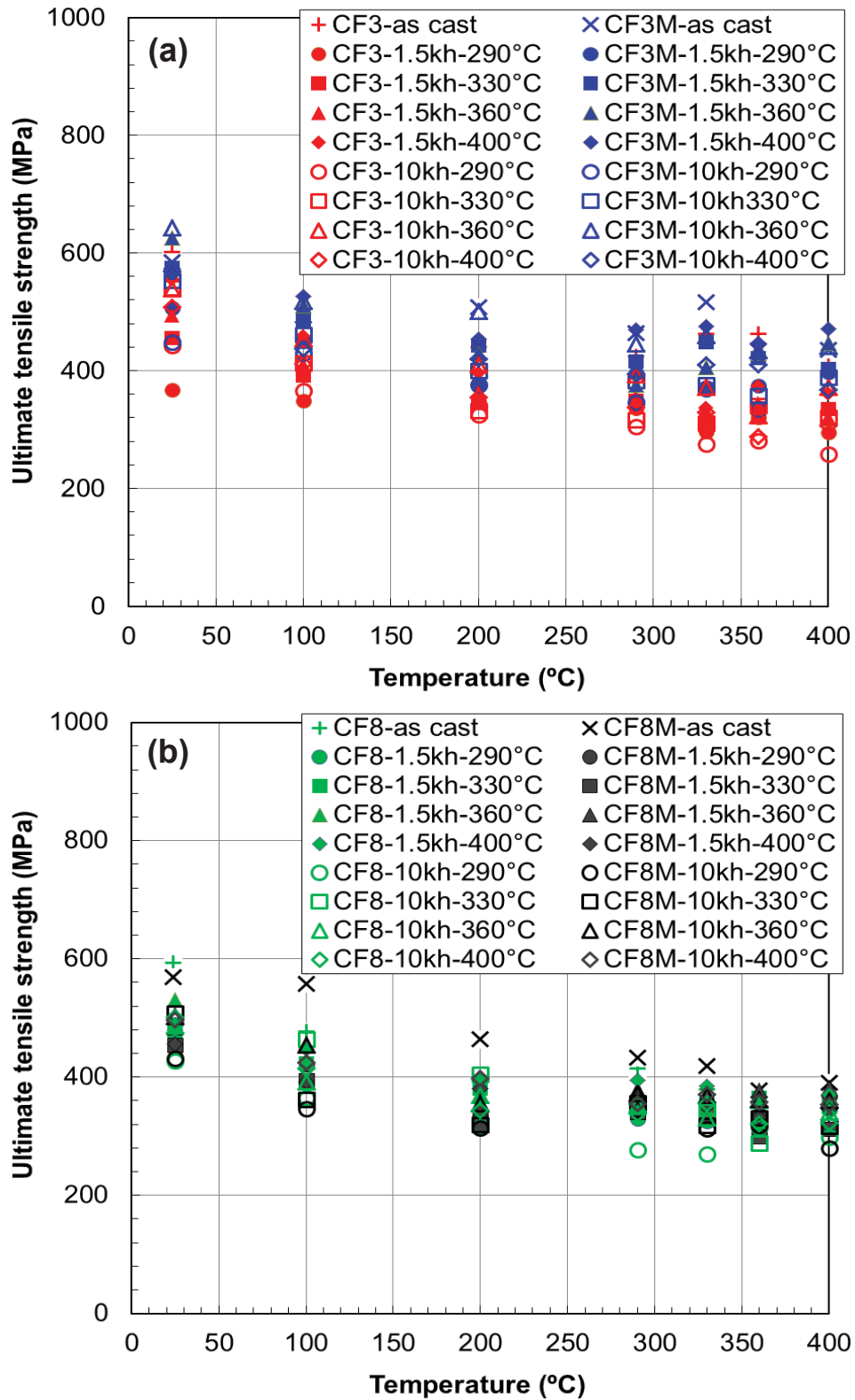Figure 3. Effect of thermal aging on yield strength (YS) in the model alloys: (a) CF3 and CF3M and (b) CF8 and CF8M

Figure 4. Effect of thermal aging on ultimate tensile strength (UTS) in the model alloys: (a) CF3 and CF3M and (b) CF8 and CF8M

3.2. Changes of UE and TE in model alloys

Figures 5 and 6 display the uniform and total elongations (UE and TE) for the aged and non-aged model CASS alloys. These UE and TE data indicate that both parameters at or above room temperature have significantly decreased after aging for 1.5 kh, then they have recovered partially after aging for 10 kh, which complies with the further reduction of strength between 1.5 kh and 10 kh, as seen in Figures 3 and 4. After the 1.5 kh aging, a few elongation data after aging present more than 50% reduction at room temperature, while the ductility reduction is typically 20–30% in the 290–400°C region, except for the CF8 alloy showing much less reduction overall. Although the reduction of ductility in the model alloys after thermal aging is significant, the less ductile CF3 and CF3M alloys still can retain high uniform ductility > ~20% over the whole test temperature range. It is also seen that the necking ductility (TE-UE) is only about 5% in average, which is close to the average value for non-aged alloys of 6%. The higher % reduction in ductility at lower temperatures, the majority of which occurred in uniform ductility, may indicate that dislocation glide becomes less linear after thermal aging [34-36].

As in the strength versus test temperature behavior, it is found that the UE and TE decrease with test temperature before they become nearly temperature independent above ~200°C. Although the overall shape of ductility versus temperature curve is retained after thermal aging, the temperature dependence becomes less steep in the low test temperature region up to 200°C. Further, after aging at 290 and 330°C for 10 kh the CF3 and CF8 alloys show steeper temperature dependence of ductility at < ~200°C, which may be because those alloys experience more age softening (i.e., more ductilization) in the lower temperature region compared to those with higher Mo content (i.e., CF3M and CF8M).

As observed in Figures 3 to 6, the 1.5 kh aging resulted in simultaneous reductions of strength and ductility. This phenomenon might be explained in association with the characteristic deformation mechanism of austenitic stainless steels, i.e., a highly linear dislocation glide. That is, more linear slip occurs at higher stress and results in higher strain hardening rate compared to a random dislocation glide [35]. Further aging to 10 kh, however, resulted in increased ductility but continued reduction of strength. This indicates that the aging mechanisms such as phase decomposition, precipitation, and segregation have been deepened to an over-aging stage that can induce ductilization of the matrix phase.

Similar to the strength behavior discussed earlier, the strength and ductility data of both aged and non-aged alloys distribute within similar band widths, though the band widths in the ductility data are much wider in percent than those of the strength data. This result again proves that the tensile deformation is not sensitive to the aging temperature, at least, in the aging up to 10 kh in the present research.
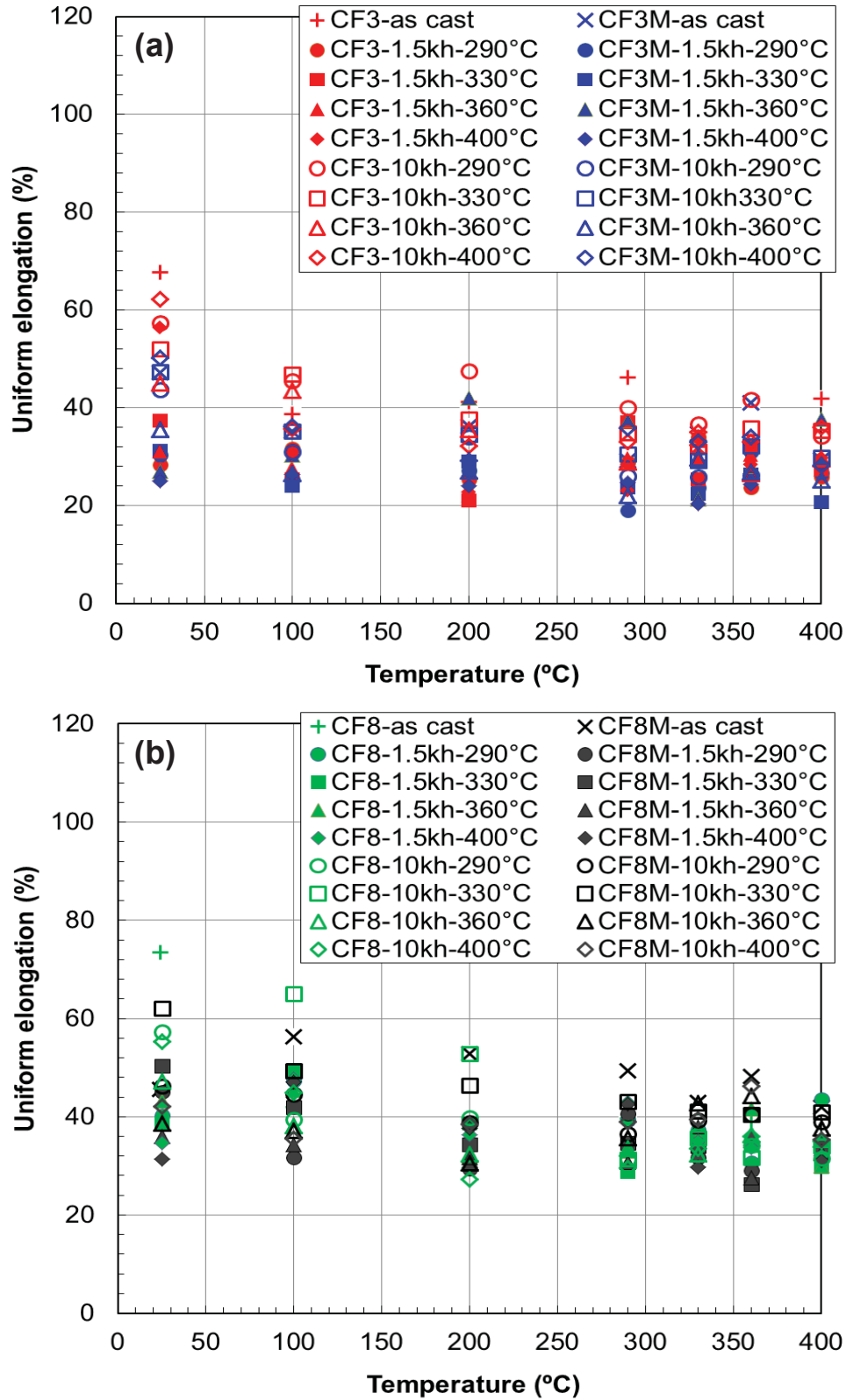
Figure 5. Effect of thermal aging on uniform elongation (UE) in the model alloys: (a) CF3 and CF3M and (b) CF8 and CF8M
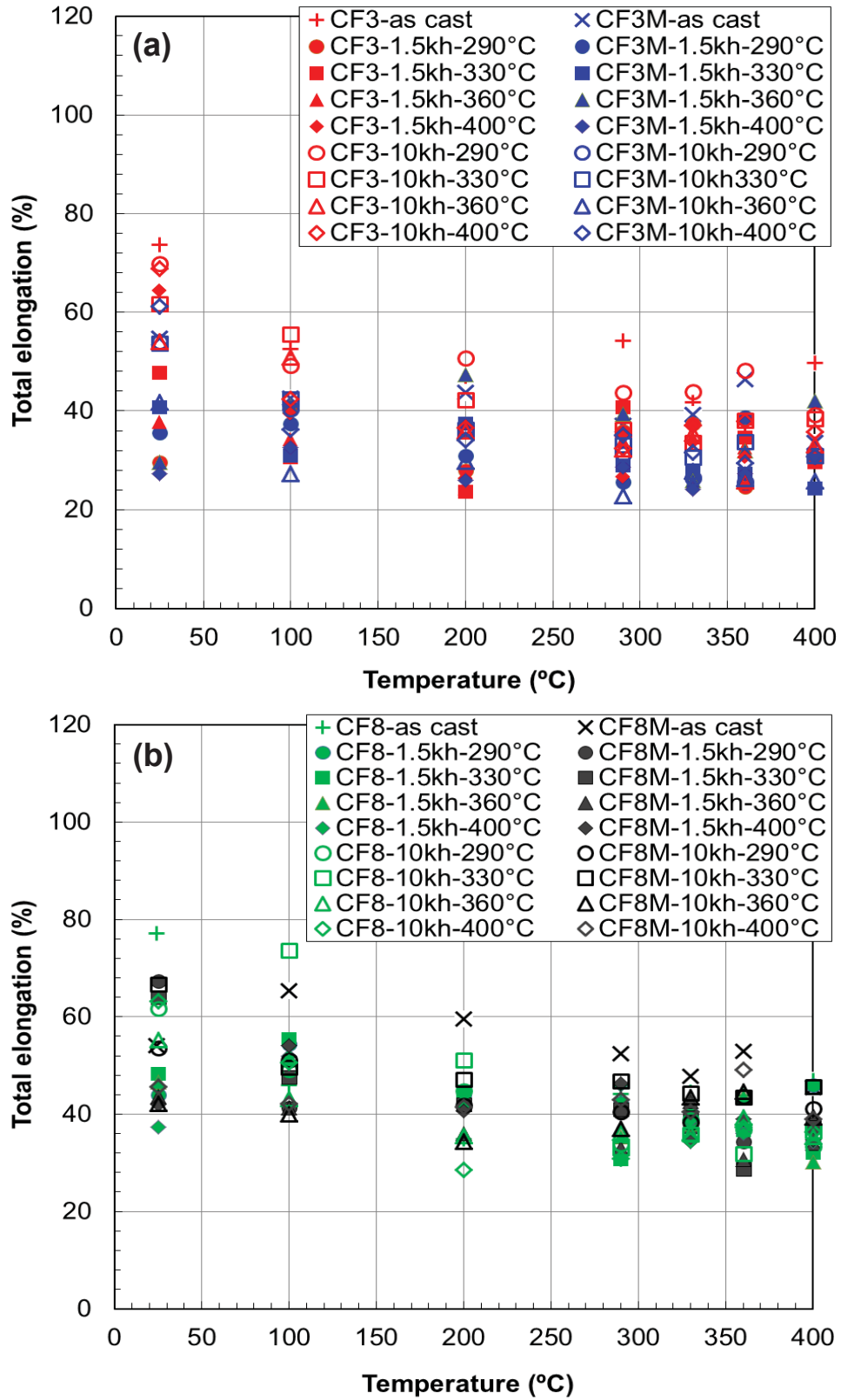
Figure 6. Effect of thermal aging on total elongation (TE) in the model alloys: (a) CF3 and CF3M and (b) CF8 and CF8M

3.3. Changes of YS and UTS in EPRI-provided alloys

The thermal aging effects on the engineering strength and ductility of EPRI-provided CASS alloys (CF8M-centrifugal/piping, CF3-centrifugal/piping, CF8-static/piping, and CF8-static/elbow) are discussed in this section. The EPRI-provided CASS alloys contain relatively high content of δ-ferrite (11–33% in the as-cast condition) and hence they are expected to show more significant property degradation on thermal aging than the model alloys with 4–16% initial ferrite content. These higher ferrite content in the EPRI-provided alloys were mainly because of the real size casting, among which the static cast elbow resulted in the highest δ-ferrite volume fraction of 33%. In Figures 7 and 8 the YS and UTS data of thermally aged and nonaged EPRI-provided CASSs are plotted against test temperature. These materials from real size components were produced through either static casting or centrifugal casting, and such a difference in processing route has resulted in easily distinguishable degradation behaviors. In general, the static cast alloys are coarser but contain higher δ-ferrite content than the centrifugal cast alloys, and the main phenomenon occurring in the δ-ferrite is clearly reflected in the tensile test results.

While the thermal aging effects are largely muted in the strength parameters of EPRI-provided CASSs, there are still a few noticeable observations. First, the YS of the centrifugal cast alloys is lower than those of the static cast alloys, as compared in Figure 7(a) against Figure 7(b). This is mainly because the δ-ferrite content is higher in the static cast alloys (in the order of 30% versus of 10%). Despite the varied amounts of δ-ferrite, however, the UTS data show little difference between the centrifugal and static cast alloys. This may be because the plastic deformation, which occurs preferably in the softer austenite phase and hence can induce higher work hardening, has compensated the age softening in the harder second phase.

Second, similarly to the model alloys, the band width of UTS for each alloy is 150–200 MPa and is roughly twice that of YS (~100 MPa). Both the YS and UTS data after aging at different temperatures for 10 kh are contained within similar band widths over the whole test temperature range. Since the property inhomogeneity would be significant within the real size CASS components, the data scatters were naturally too large to discern the effect of aging temperature.

Third, Figures 7 and 8 commonly show that the thermal aging for 10 kh has not changed the temperature dependence of strength in the EPRI-provided alloys: the aging treatment has negligible effect on the general temperature dependence of strength, in which both the YS and the UTS decrease with test temperature at similar rates but become nearly temperature-independent in the aging temperature range of 290–400°C.

Finally, it is pointed out that the effect of different alloying compositions, if any, is overshadowed by the effect of δ-ferrite content that is primarily determined by casting method. A comparison of the strength data for the centrifugal cast CF8M alloy and static cast CF8 alloy indicates that the static cast alloy has yield strengths that are approximately 50 MPa higher than those of the CF8M. This difference is, however, evident only in the YS data as seen in Figure 7 but almost disappears in the UTS data, Figure 8. This behavior remained unchanged after the thermal aging treatment.
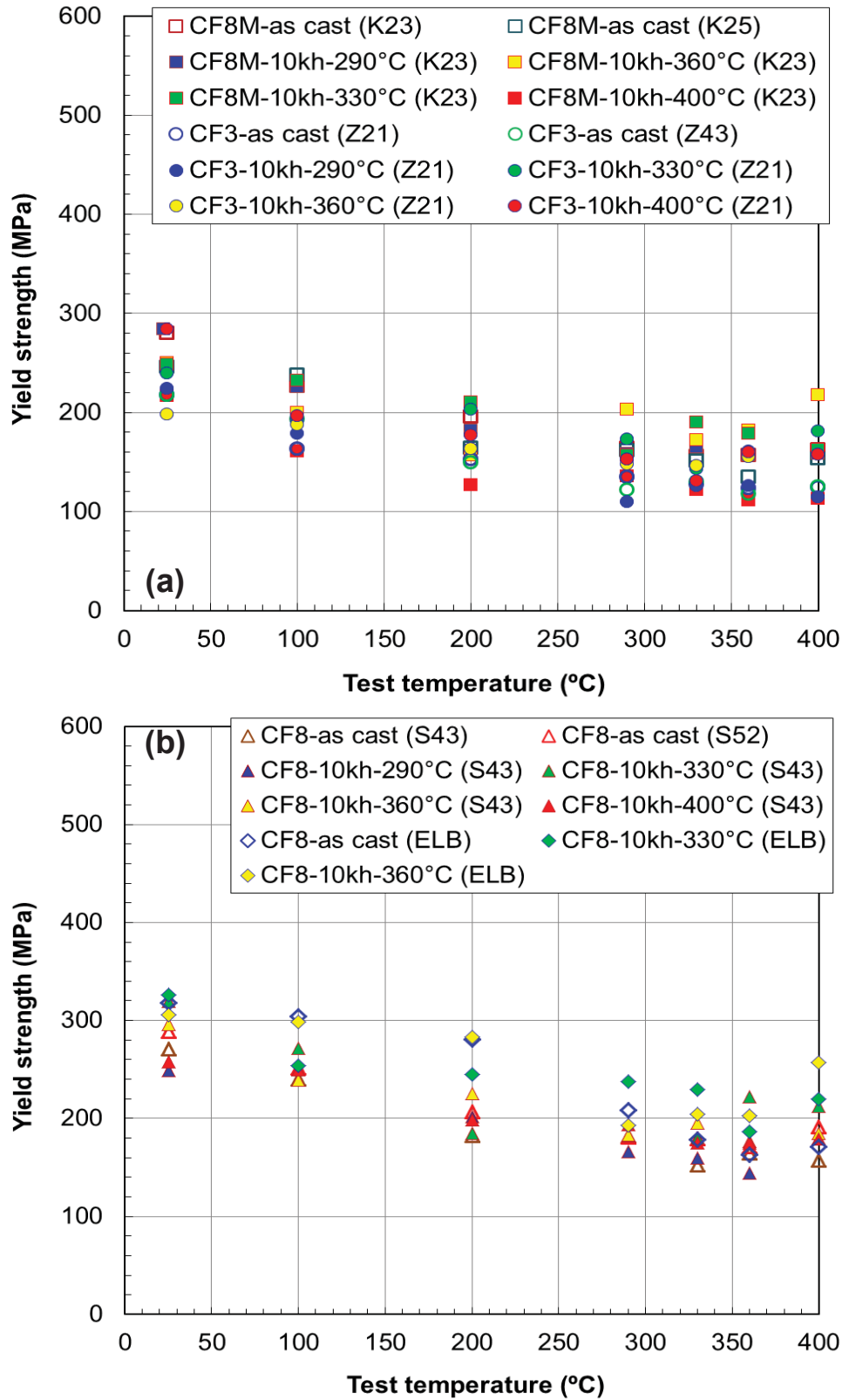
Figure 7. Effect of thermal aging on yield strength (YS) in the EPRI-provided alloys: (a) CF8M and CF3 from centrifugal cast pipings and (b) CF8 from static cast piping and elbow.
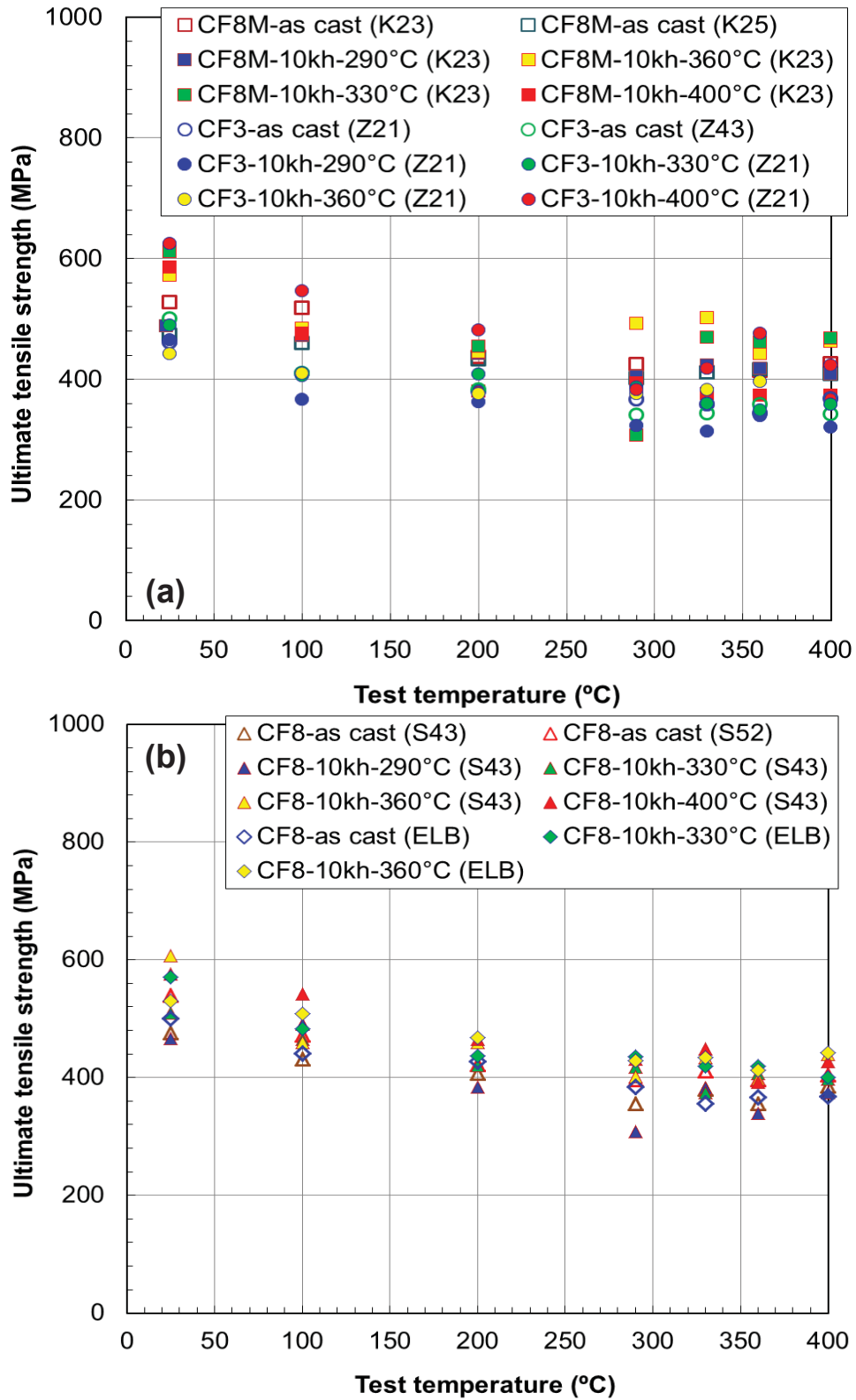
Figure 8. Effect of thermal aging on ultimate tensile strength (UTS) in the EPRI-provided alloys: (a) CF8M and CF3 from centrifugal cast pipings and (b) CF8 from static cast piping and elbow.

3.4. Changes of UE and TE in EPRI-provided alloys

Figures 9 and 10 display the uniform and total elongations (UE and TE) of the aged and non-aged EPRI-provided alloys. These ductility datasets indicate that these CASS alloys slightly lose their ductility during the 10 kh aging although the changes are too small and scattered to be seen as a consistently evident trend. The large data scatters seemingly due to material inhomogeneity from ductility data bands as wide as 40% in both the UE and TE datasets. As in the model alloys, the variations in ductility that may be caused by the difference in alloying elements and aging conditions are not clearly discernable. Despite the wide scatters and some aging-induced reductions, the vast majority of the UE and TE values remained above ~20% over the whole test temperature range of 25–400°C, while just a few ductility data are slightly below the 20% mark only in the aging temperature range. One case that shows a noticeable ductility reduction is the static cast CF8-elbow material, which has the highest δ-ferrite content of 33%. Both ductility parameters of this material show little temperature dependence over the whole test temperature range.

It is also noted that both the UE and the TE of the centrifugal cast CF8M and CF3 alloys are about 10% higher at room temperature and 100°C than those of the stable cast CF8 piping and elbow materials, but the difference becomes negligible at higher temperatures. Except for this difference, the overall test-temperature dependence of ductility for these alloys is similar to those of model alloys both before and after thermal aging.
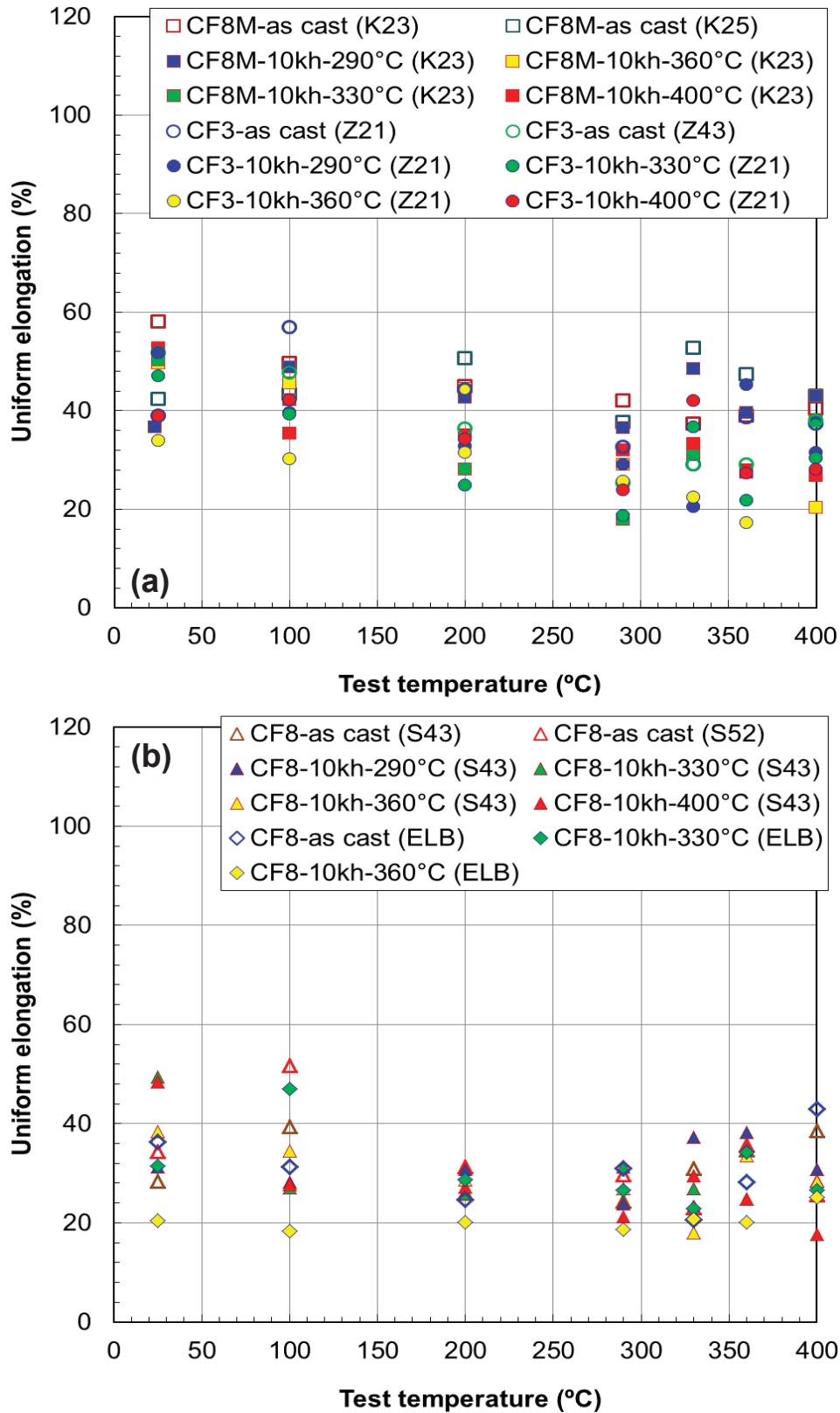
Figure 9. Effect of thermal aging on uniform elongation (UE) in the EPRI-provided alloys: (a) CF8M and CF3 from centrifugal cast pipings and (b) CF8 from static cast piping and elbow.
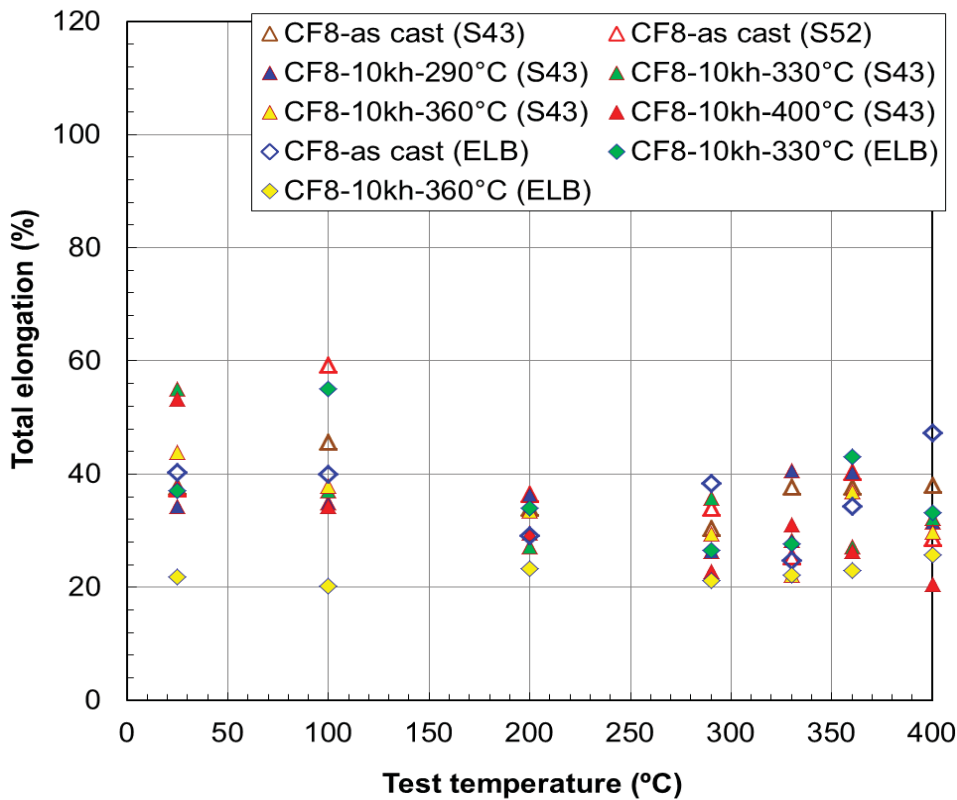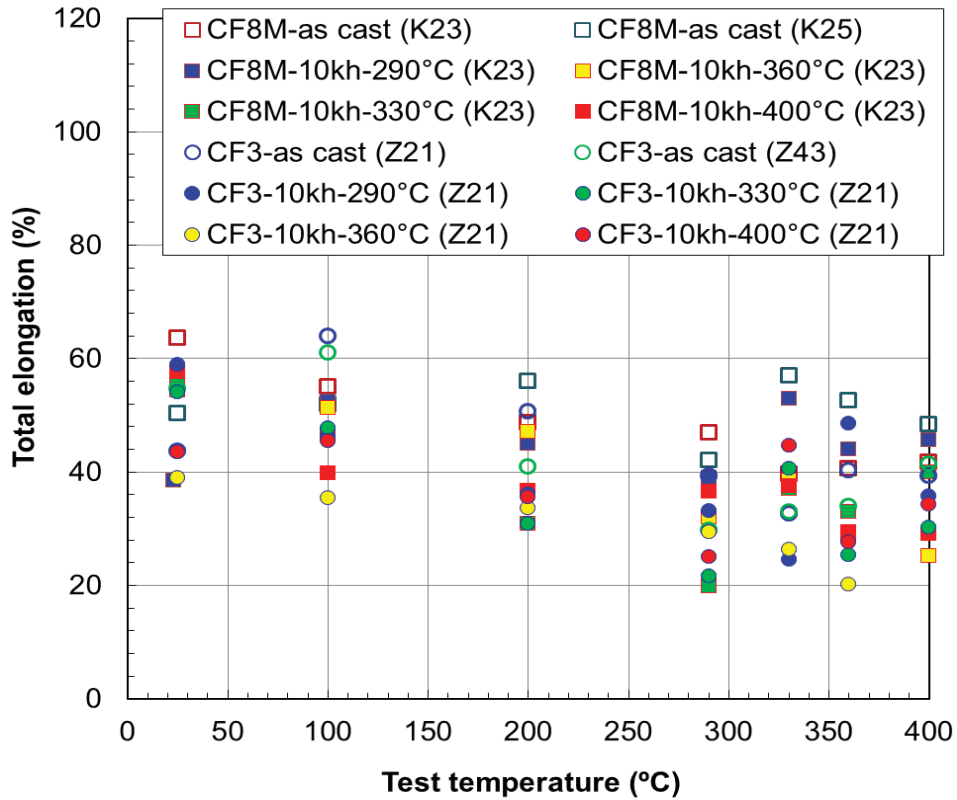
Figure 10. Effect of thermal aging on total elongation (TE) in the EPRI-provided alloys: (a) CF8M and CF3 from centrifugal cast pipings and (b) CF8 from static cast piping and elbow.

4. EFFECTS OF THERMAL AGING ON CHARPY IMPACT ENERGY

4.1. Impact energy transition curves of model alloys

The impact energy datasets and corresponding fitted hyperbolic tangent curves are presented in Figure 11 for the four model alloys: (a) through (d) for CF3, CF3M, CF8 and CF8M, respectively. Since these CASS alloys contain relatively low content of δ-ferrite (< 16%), the effect of thermal aging on mechanical properties including Charpy impact energy is expected to depend on the well-known significant degradation of ferrite phase but with a large influence from the relatively mild degradation or even ductilization of austenite matrix.

Before aging the CF3 and CF8 alloys have 20–25% higher impact energy in upper shelf region than their molybdenum containing counterparts, CF3M and CF8M, and such a difference persisted after aging. It is also noted that the impact energy of the nonaged CASS alloys do not reach their lower shelves, as the measured absorbed energies at the lowest test (liquid nitrogen) temperature were much higher than the expected lower shelf value of $\leq$ 20 J.

Figures 11(a) through 11(d) show that the model alloys experience significant reduction of impact energy during the short-term aging for 1.5 kh, which are measured as significant reductions of upper shelf energy and large positive shifts of transition temperature [31]. Among the four CASS materials, the CF3M alloy experienced the most significant but gradual degradation during the short term (1.5 kh) aging [31], but the further degradation was highly depending on aging temperature. At the same time, the CF8 alloy showed similar degree of impact energy reduction, but the shift of transition temperature region was much smaller. Another notable difference between these two alloys is that the shift of ductile-brittle transition region and the reduction of impact energy occur gradually with aging temperature in CF3M, but they are less sensitive to the aging temperature in CF8. It is found, however, that the continued aging to 10 kh has resulted in a wide range of property changes including both the impact energy recovery and the further degradation: For example, the further aging at either 290 °C or 330 °C after 1.5 kh has caused significant recovery of impact energy in CF3 and CF3M alloys. The impact energy of CF3M alloy continued to decrease during aging at 360°C.
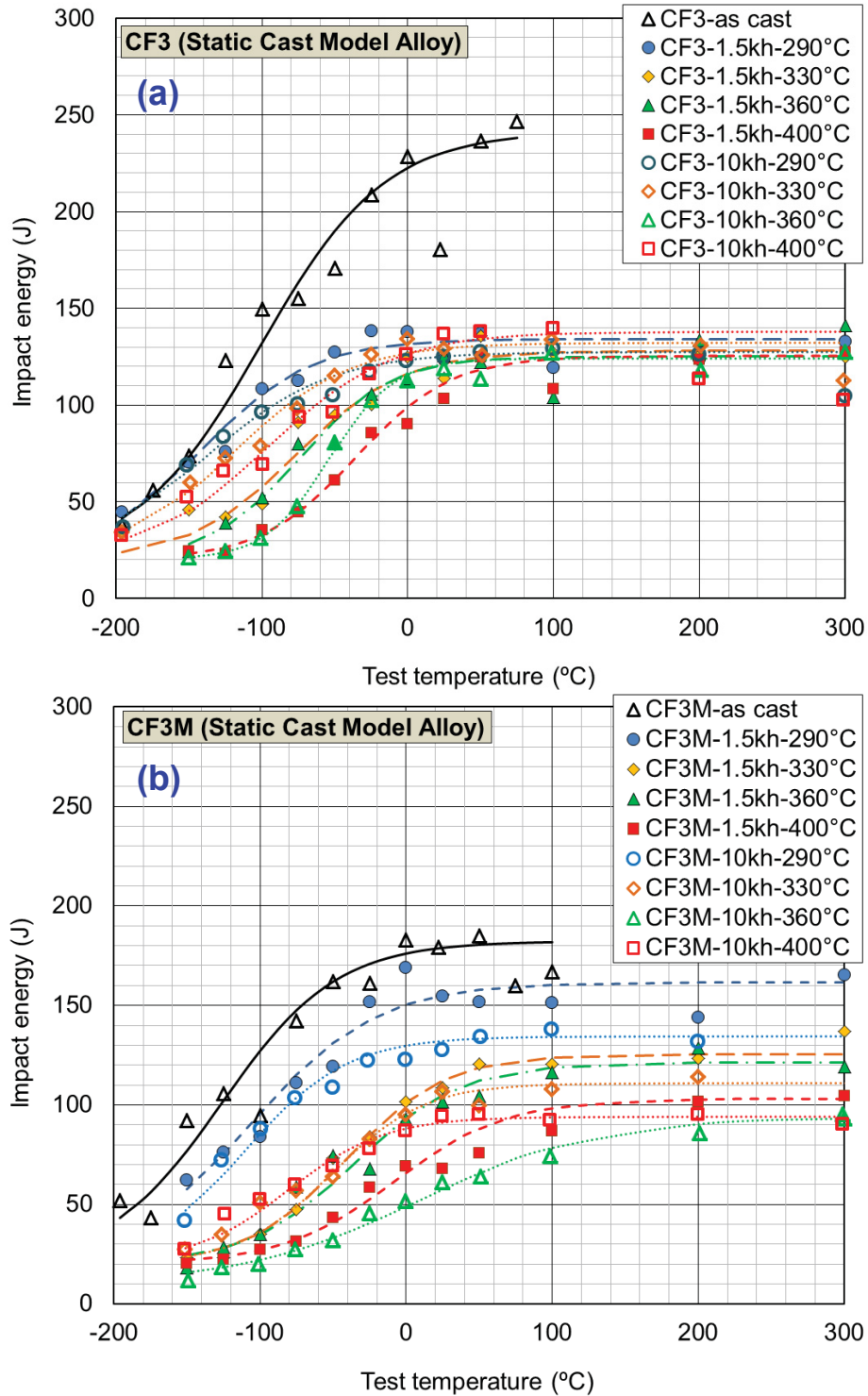
Figure 11. Temperature-transition curves of Charpy impact energy for (a) CF3 alloy and (b) C3M alloy after aging for 1.5 kh and 10 kh.
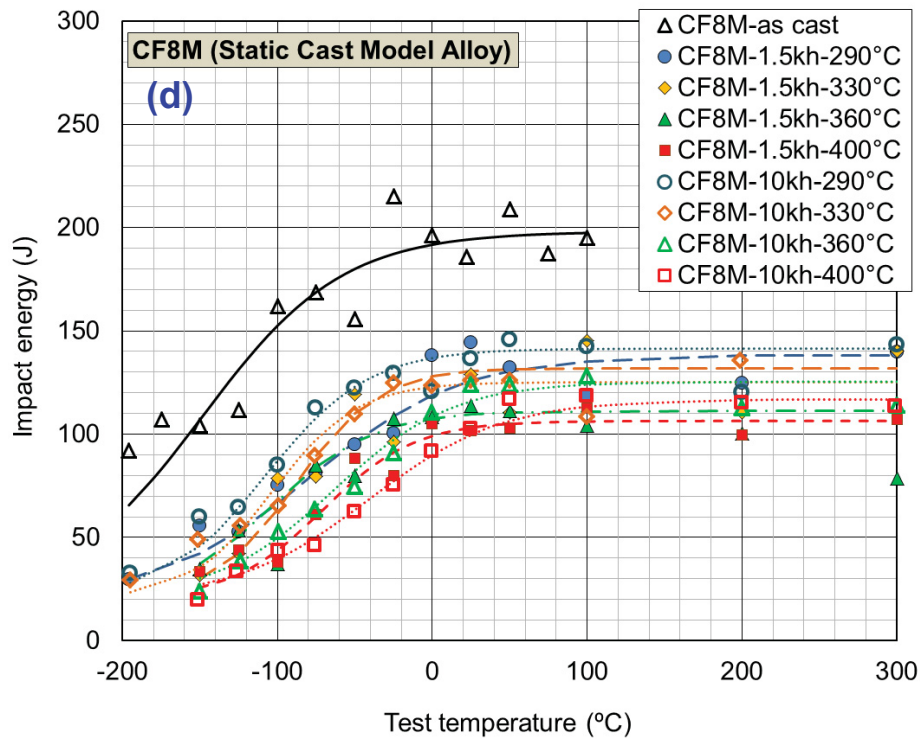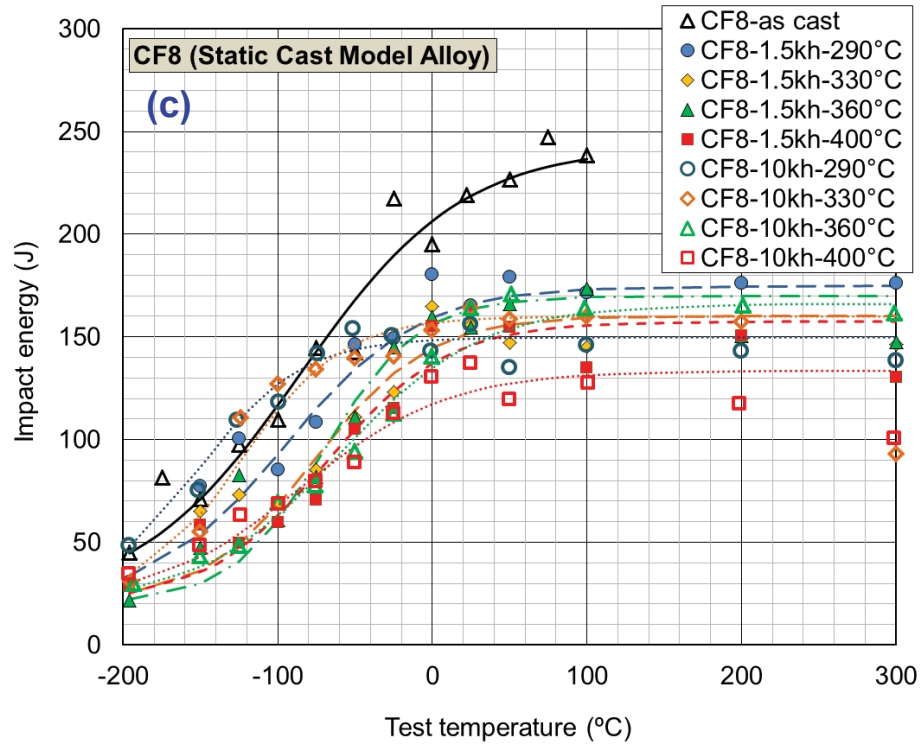
Figure 11. Temperature-transition curves of Charpy impact energy for (c) CF8 alloy and (d) C8M alloy after aging for 1.5 kh and 10 kh.

4.2. Aging effect on USE and DBTT in model alloys

The impact energy transition parameters, i.e., USE and DBTT, determined through the hyperbolic tangent function analysis are presented in Figures 12 and 13. Overall, the USE data show insignificant aging temperature dependence while the DBTT data exhibit more aging temperature dependence and complex degradation behavior. Some noticeable details are:

First, the as-cast CF3 and CF8 alloys have high USEs of about 240 J and the as-cast CF3M and CF8M alloys slightly lower USEs of ~180 J and ~200 J, respectively. For all model alloys, USE decreased significantly after thermal aging. The molybdenum containing alloys (CF3M and CF8M) showed evident aging temperature dependence while the decrease of USE in CF3 and CF8 was rather sudden in the 1.5 kh aging and then showed little aging temperature dependence up to 10 kh. It was initially predicted that the USE after aging at the highest aging temperature of 400°C would be the lowest for each alloy and the reduction of USE by thermal aging more significant in the molybdenum containing alloys. It is observed, however, that the maximum percent reduction of USE measured after aging is limited to < 50%, and that it is nearly independent of alloy composition and does not always occur at the highest aging temperature: the maximum reductions of USE for all model alloys fall within a narrow range of 43–49%. The lowest USE (94 J) was measured in the CF3M alloy after the highest degree of aging (at 360 and 400 °C for 10 kh), which corresponds to a 48% reduction from 182 J.

Second, as shown in the contrast between the small aging effect in tensile strength and the significant reduction in tensile ductility, the degree of thermal aging degradation is not uniform among the impact property parameters. That is, the DBTT is significantly more sensitive to the thermal aging condition and alloy composition when compared to the USE behavior. The CF3M alloy shows its DBTT shifted above room temperature (+9°C or ΔDBTT = +135°C) after aging at 360°C for 10 kh. The smallest shift (ΔDBTT), +17, is found in the CF8 alloy after aging at 400°C for 10 kh. This CF8 alloy, having relatively high carbon content but low molybdenum content, demonstrated the best resilience to thermal degradation among the alloys, primarily because it has the lowest δ-ferrite content (~5%) among the model alloys.

Third, the decrease of DBTT after increase (see the CF3-10kh-400°Ccase for example) is believed to result from over-aging. For all model CASS alloys, the aging recovery of DBTT (or negative shift of DBTT) is particularly evident in the low temperature (290 and 330 °C) aging. It is a highly notable that no alloys show any evidence of recovery after aging at 360 °C. These may indicate that the degradation mechanisms are not highly activated at the two lower aging temperatures while the softening mechanisms in the austenite matrix are relatively more active. Meanwhile, the ductilization due to over-aging appears to be not significant in USE measurements.

Fourth, it is noted that the DBTT change in thermal aging is dependent on other transition parameters (e.g., USE) as well as on the thermal degradation behavior itself; that is, the small decrease in DBTT after a mild aging (e.g., CF3-1.5kh-290°C) is partially due to the large decrease of USE. As mentioned in section 2.4, this is a drawback from the simplest definition of DBTT. A toughness parameter at a fixed temperature, such as T_{41J}, is recommended to be used in scientific description.
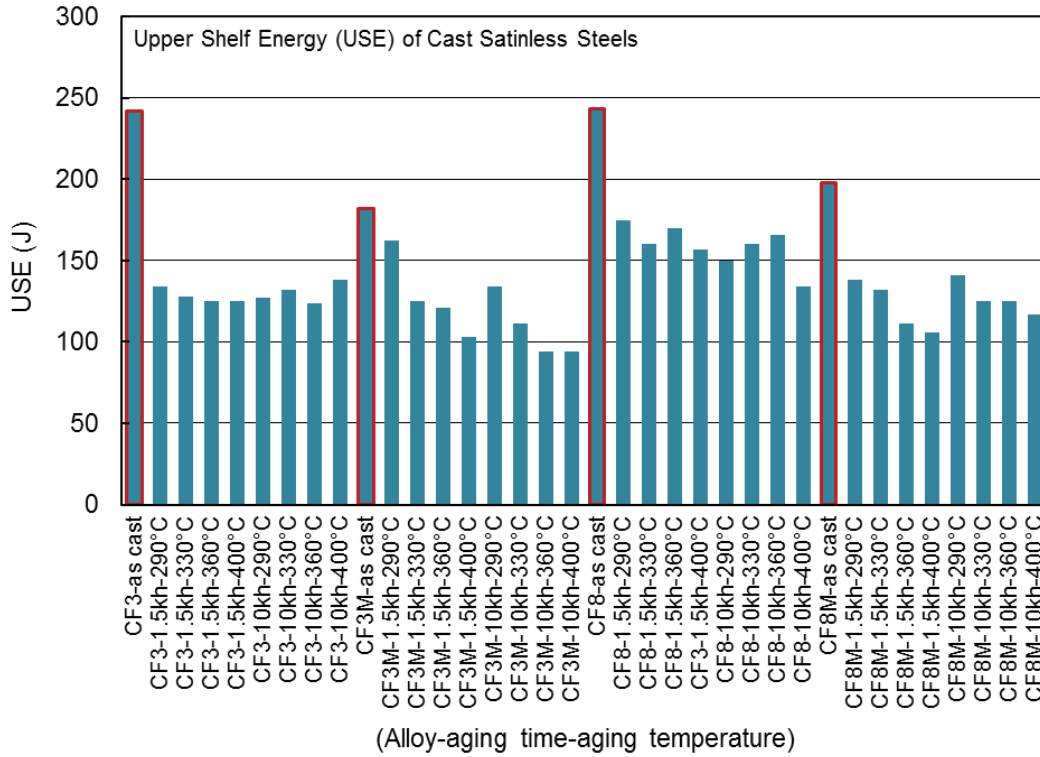
Figure 12. Effect of 1.5 kh and 10 kh thermal aging on upper shelf energy (USE) in model alloys
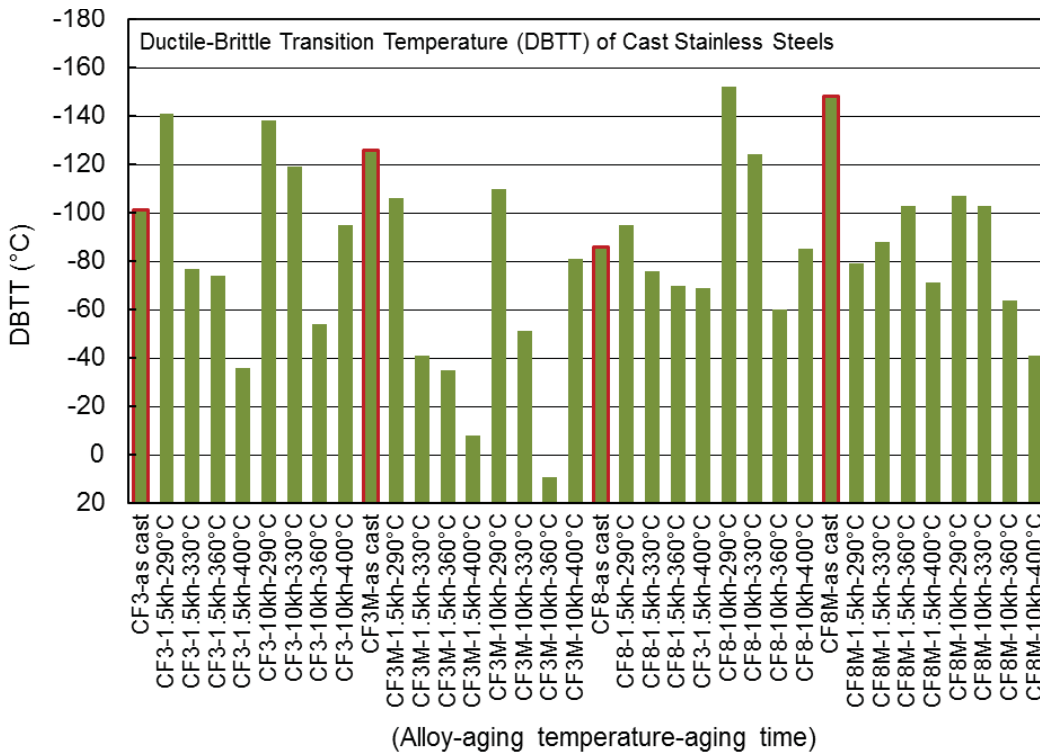

Figure 13. Effect of 1.5 kh and 10 kh thermal aging on ductile-brittle transition temperature (DBTT) in model alloys

4.3. Impact energy transition curves of EPRI-provided alloys

The absorbed energy versus test temperature data of aged and nonaged EPRI-provided CASSs are presented in Figures 14(a) and 14(b), where the datasets and their best-fitting hyperbolic tangent curves are compared in two separate groups of centrifugal cast materials and static cast materials, respectively. The group of four EPRI-provided alloys consists of CF3-centrifugal cast piping (Z21), CF8M-centrifugal cast piping (K23), CF8-static cast piping (S43), and CF8-static cast elbow (ELB) materials. It is known that the centrifugal cast alloys usually have lower δ-ferrite content and finer microstructures than the static cast alloys due to relatively higher cooling rates in casting [3]. Slow cooling of the thick (~20 cm) elbow and higher molybdenum content are additional parameters that might adversely affect impact properties before and after aging in CF8 (ELB).

As compared in Figure 14(a), the centrifugal cast CF3 alloy (Z21) has much higher impact energy than the centrifugal cast CF8M alloy (K23) in as-cast condition. This difference prior to aging should be because much higher molybdenum content is contained in CF8M than in CF3 (2.51% vs. 0.14%). The low C content in CF3 might also help having such extraordinary toughness. As a common behavior for both alloys, the impact energies measured above the upper transition temperatures were higher after the 290 °C aging than those before aging, while the aging still increased the transition temperature region. Another common behavior observed for these two centrifugal cast alloys is that the biggest decrease of impact energy is measured in the specimens after aging at 360 °C, not at the highest temperature of 400 °C. This was also observed in three model alloys (i.e., CF3, CF3M, and CF8) after aging for 10 kh.

The two static cast CF8 alloys also show significant difference in the level of impact energy and transition behavior, in Figure 14(b). The CF8 elbow material has higher impact energies before aging but exhibits much lower values after aging when compared to those of CF8 piping material (S43). The absorbed energies measured in the CF8-elbow material after 10 kh aging are lower than 100 J up to 100 °C. Such a profound degradation might be caused by the large amount of δ-ferrite (33%) as well as by the coarse microstructure and segregation due to slow cooling. The CF8 piping material (S43) had the lowest pre-aging impact energies with a high content of δ-ferrite (~25%) and experienced a significant aging effect in the Charpy curve, but the change was much smaller than CF8 (ELB).
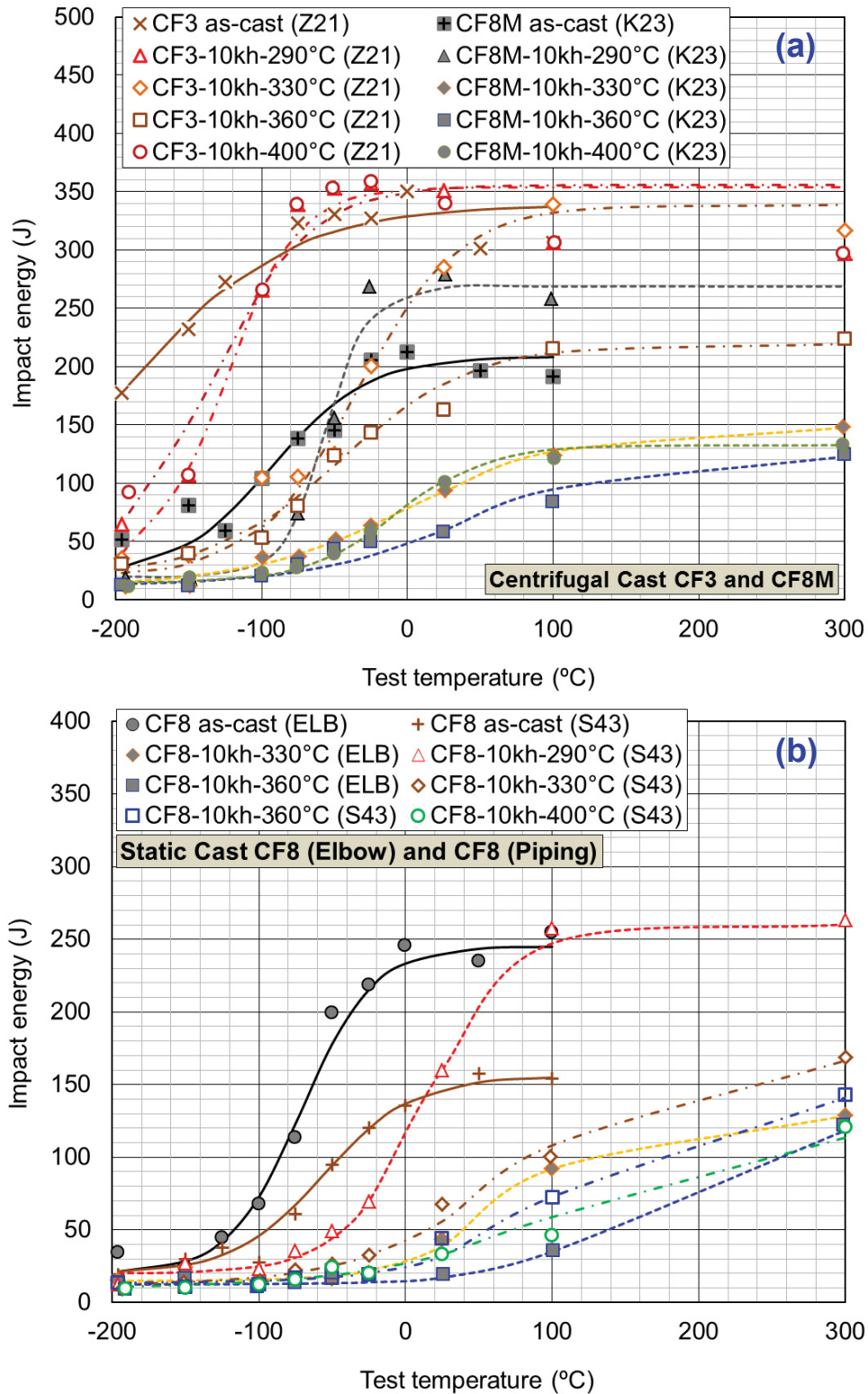
Figure 14. Temperature-transition curves of Charpy impact energy for EPRI-provided CASSs:
(a) Centrifugal cast CF8M and CF3 alloys and (b) Static cast CF8 alloys after aging for 10 kh.

4.4. Aging effect on USE and DBTT in EPRI-provided alloys

The results of regression analyses are summarized in Figure 15 and Figure 16 for the USE and DBTT of EPRI-provided alloys, respectively. Before aging the USE of the centrifugal cast CF3 is the highest among the CASS alloys. The effect of aging on impact toughness in ductile region is limited in this alloy as the USE data show little change except for the value after 360°C. Comparison of the USE data in Figure 15 indicates that the molybdenum content can cause the biggest effect on USE before aging but the δ-ferrite content is the biggest factor determining the reduction of USE: the CF8M alloy with 2.51% Mo has the lowest USE before aging, but the reduction of USE by aging is larger in the static cast CF8 alloys with 25 and 33% δ-ferrite.

Figure 16 compares the DBTT data of four EPRI-provided materials in various aging conditions. It is found that the shift of DBTT varies widely, particularly with whether it is static or centrifugal casting. The centrifugal cast CF3 (from Z21 pipe ring) showed significant DBTT shifts by aging, though thermal recovery (i.e., decrease of DBTT) became apparent after aging at 360 and 400°C. The CF8M alloy (K23, centrifugal cast) also indicated the recovery behavior in the 400°C aging after its DBTT increased well above room temperature by 360°C aging. It is noted that much higher initial DBTT was measured in this Mo-doped CF8M alloy, although the degradation-recovery behaviors afterward are similar for both materials. Both of these centrifugal cast alloys have similar δ-ferrite content of ~12%. On the other hand, the static cast CF8 alloys have much higher δ-ferrite content of 23–33% on average and display correspondingly more significant degradation. Both of the static cast materials, CF8 (S43 piping) and CF8 (elbow), display profound and temperature-dependent shift of DBTT after aging. All the post-aging DBTT data evaluated for these two materials are at or above room temperature, which can be regarded as embrittled. Both the high Mo content and the high δ-ferrite content are believed to be the prerequisite factors that can induce significant degradation or embrittlement.
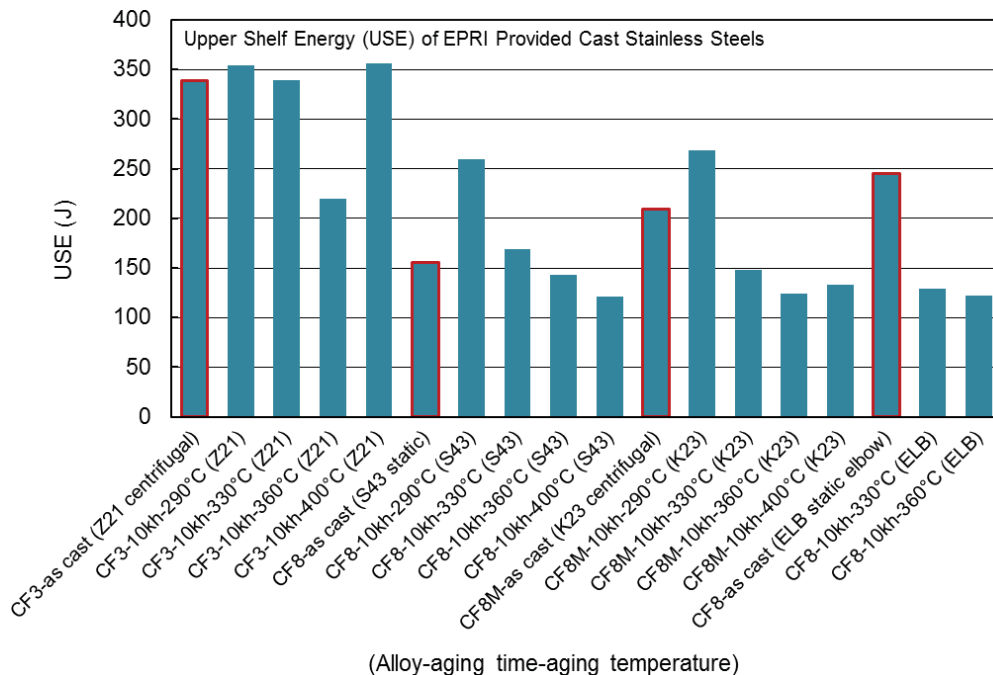

Figure 15. Effect of 10 kh thermal aging on upper shelf energy (USE) in EPRI-provided alloys
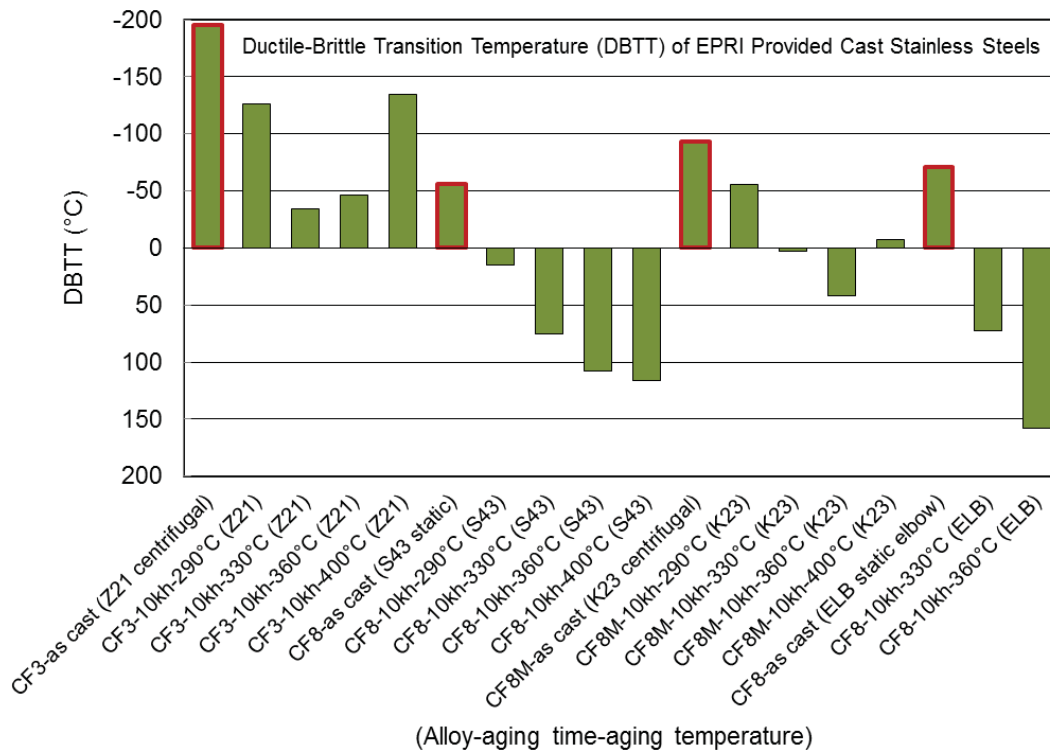
Figure 16. Effect of 1.5 kh and 10 kh thermal aging on ductile-brittle transition temperature (DBTT) in EPRI-provided alloys

5. MICROSTRUCTURAL EVOLUTION WITHIN FERRITE PHASE

Four primary microstructural feature changes appear in the alloys to various extents after 1.5 kh and 10 kh of aging: spinodal decomposition, G-phase precipitation, segregation of solute, and precipitation of carbides. The first two take place within the ferrite phase while the latter two take place at the ferrite/austenite interphase boundary. There is a dependence of these feature changes on chemical composition, aging temperature, and aging time.

5.1. Visualization of spinodal decomposition and G-phase precipitation in ferrite phase of model CASS alloys

Spinodal decomposition of the ferrite phase into Fe-rich α and Cr-rich α` is a well-known characteristic of the microstructural evolution of ferrite during thermal aging; though the dependence on aging time, aging temperature, and chemical composition is less understood. Figure 17 shows STEM-BF images of all four model CASS alloys after 1.5 kh of aging at either 330°C or 400°C in regions that are several hundreds of nanometers from any interface or grain boundary. Spinodal decomposition along with G-phase precipitation are observed in all the alloys at a temperature of 400°C as evidenced by the mottled contrast; however, it is not noticeable within STEM-HAADF or BF imaging in the as-cast condition or after aging at 330°C. The G-phase, is a Ni/ Si-rich phase that precipitates from the ferrite phase. Due to the fine scale to the microstructural features shown in Figure 17, the presence of G-phase precipitation could not be positively identified over that of the α/α' decomposition through STEM imaging, though this will be shown in the following APT work. However, spinodal decomposition or G-phase

36

precipitation could be observed in the as-cast materials or in the materials aged at 330°C for 1.5 kh using STEM-HAADF/ BF imaging.
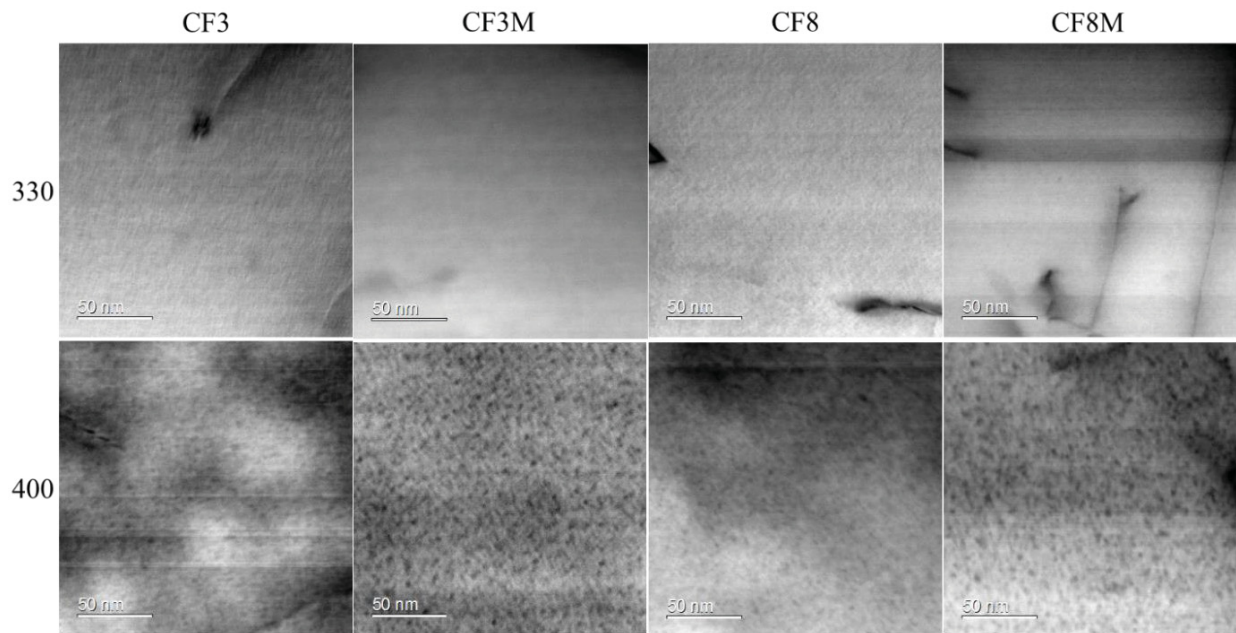

Figure 17. BF-STEM images of spinodal decomposition after 1.5 kh of aging at 330°C and 400°C in CF3, CF3M, CF8, and CF8M alloys.

Further characterization via APT was utilized to determine the extent of spinodal decomposition and G-phase precipitation within ferrite regions of the alloys as a function of chemical composition and aging conditions. An example of spinodal decomposition and G-phase precipitation as a result of high temperature aging is shown in Figure 18 in a CF8M aged for 1.5 kh at 400°C, where 2D concentration plots show the variation in chemical composition within a 1 nm slice of the APT tip. The APT concentration plots show decomposition of Fe and Cr into two separate regions, while Ni, Si, and Mn cluster together (along with Cu and P not shown here), and Mo tends to segregate to the Cr-rich regions and the Ni/Si-rich clusters. The Ni/Si-rich clusters are the G-phase while the Fe-rich and Cr-rich regions are α and α`, respectively. The Fe and Cr-rich regions are approximately 3-5nm in size with the G-phase precipitates approximately the same size. The decomposed regions are interconnected, particularly with respect to Fe, while the Cr-rich regions have some separation. The same type of 2D visualization of the as-cast CF8M alloy and the CF8M alloy aged at 330°C for 1.5 kh are in Figures 19 and 20, respectively. In both cases, there is a small amount of decomposition of Cr from Fe, but to a much smaller extent than the 400°C aged sample. Interestingly, there is a good amount of chemical variation across both the as-cast and 330°C aged samples, but the composition range for each element is about 3-5 times smaller for the as-cast case.

Figure 18. APT 2D concentration maps with 1nm^3 voxels for ferrite in a CF8M steel aged for 1.5 kh at 400°C. Area is 45nm X 130nm and sampled 1nm in depth. Blue represents lower concentration and red represents higher concentration of each element. Concentration range is noted above/ below each panel.
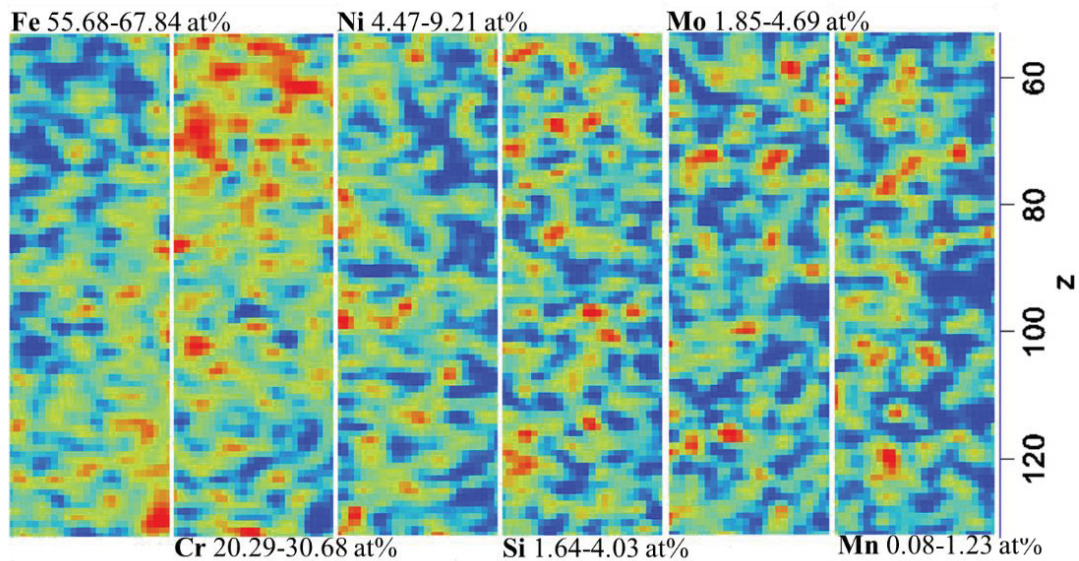
Figure 19. APT 2D concentration maps with 1nm^3 voxels for ferrite in as-cast CF8M steel. Area is 25nm X 80nm and sampled 1nm in depth. Blue represents lower concentration and red represents higher concentration of each element. Concentration range is noted above/ below each panel and is much smaller for each element compared to Figure 8.

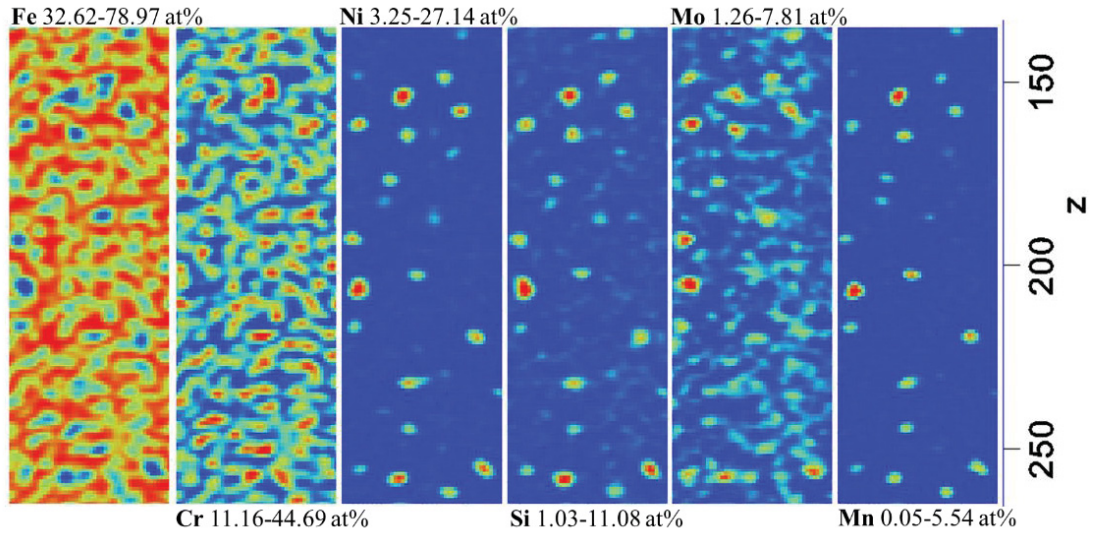*Figure 20. APT 2D concentration maps with 1nm³ voxels for ferrite in a CF8M steel aged for 1.5 kh at 330°C. Area is 30nm X 100nm and sampled 1nm in depth. Blue represents lower concentration and red represents higher concentration of each element. Concentration range is noted above/ below each panel.*
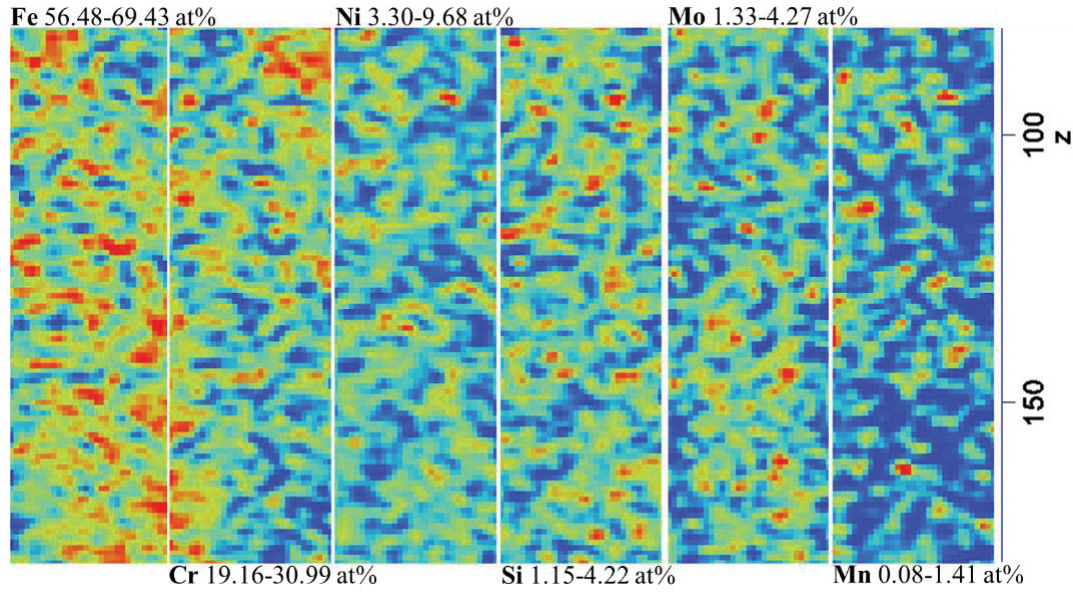
5.2. Quantification of spinodal decomposition within ferrite phase of model CASS alloys

While these 2D concentration plots provide visualization of the spinodal decomposition and G-phase precipitation, radial distribution functions (RDF) allow for direct quantization of the effects of aging temperature and chemistry on these features. With the knowledge how each element tends to segregate during aging, the effects of aging temperature and composition can be determined. For spinodal decomposition, the Cr RDFs for each alloy at different aging temperatures after 1.5 kh and 10 kh of aging is shown in Figure 21. For the 400°C, the high Mo alloys were observed to have the greatest Cr segregation, though it appears that the Mo and C may have a synergistic effect as the CF3M alloy has slightly greater Cr amplitude than the CF8M alloy and the CF3 alloy has a slightly greater Cr amplitude than the CF8 alloy; though they are only small differences. Also interestingly, the dependence on aging temperature is large among all four temperatures. After aging at 290°C, there is very little change in segregation behavior from the as-cast condition. The amount of change is only slight after 330 and 360°C. The same attributes – low C and high Mo – continue into aging after 10 kh. Also, aging at 360°C for 10 kh approaches the same amount of segregation that was seen after 1.5 kh aging at 400°C. As will be noted later, this is in stark contrast to G-phase precipitation which escalates rapidly after 10 kh aging compared to 1.5 kh aging.
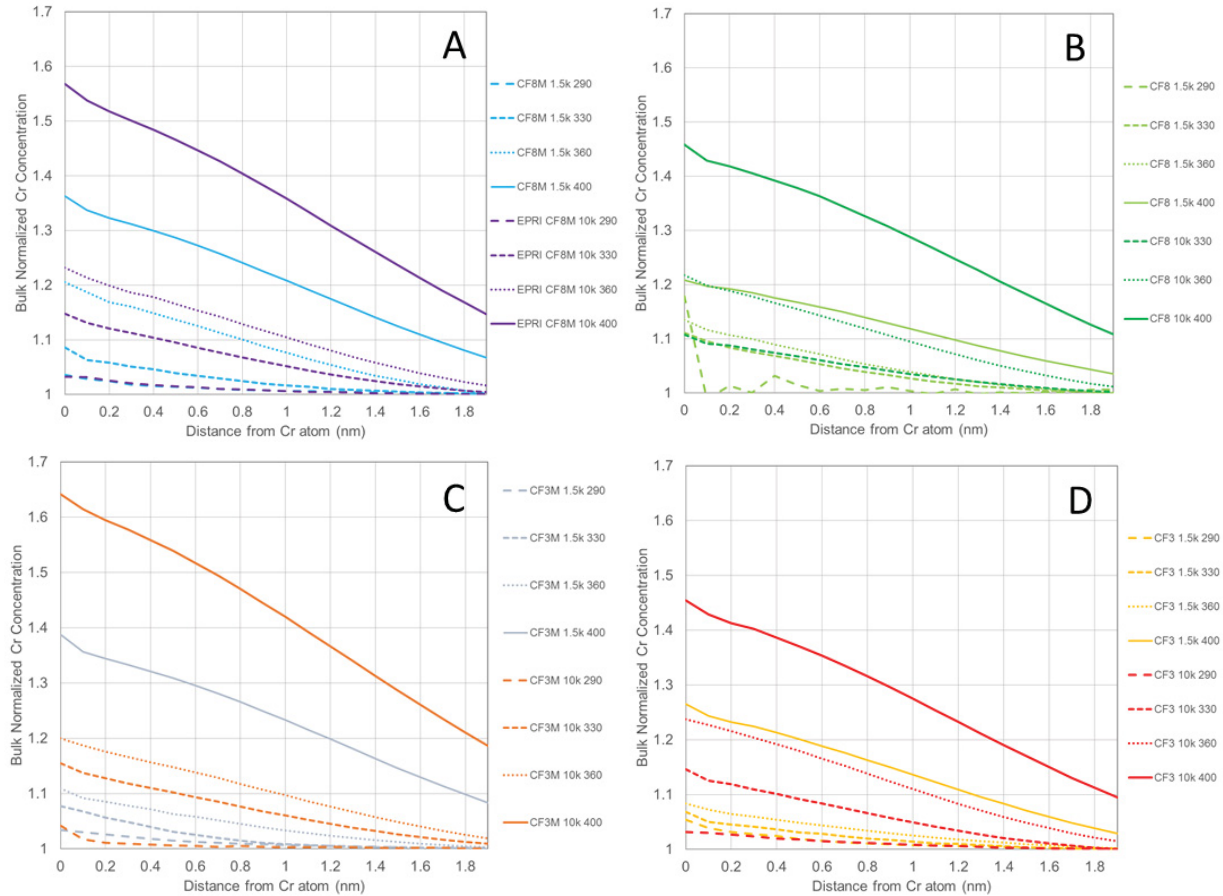
Figure 21. Radial distribution function for Cr Concentration from Cr atoms in (a) CF8M, (b) CF8, (c) CF3M, and (d) CF3 after 1,500 hours and 10,000 hours thermal aging

To further quantify the extent of spinodal decomposition and compare the different alloys, Cr RDFs are taken out to a distance of 8nm to identify a second peak after the 0nm RDF peak, which specifies a statistically nearest distance between two Cr-rich regions in three-dimensions, and thus in this case, indicates the wavelength of the spinodal decomposition and the 0nm peak is correlated to the compositional amplitude of the decomposition [27]. These comparisons are made in Figure 22, where the Cr-Cr RDF is shown for each alloy at 400 °C, as well as all the aging temperatures for CF8M. Similar conclusions are made compared to Figure 21; the wavelength and compositional amplitude of the decomposed regions follow the same trend. The CF3M, with high Mo and low C content, undergoes the most decomposition with a second peak of 6.6nm at 400 °C. The other high Mo alloy, CF8M, also undergoes a similar, though slightly less, amount of decomposition with a second peak at 6.6nm at 400 °C and 4.8nm at 360 °C. The CF8 at 400 °C has the smallest amplitude of the four alloys and interestingly, has no second peak; though there is a small second peak in the same alloy aged at 360 °C of 4.4nm (not shown). This could be due to a combination of the small volume of the APT tip along with the already small degree of decomposition in this particular alloy. The CF3 alloy at 400 °C, like the other low Mo alloy CF8, has a smaller amount of decomposition compared to the high Mo alloys with a second peak at only 5.8nm. Unsurprisingly, the second peak of the CF8M alloys at 330 °C is very small and nonexistent at 290°C. This delay of segregation until about 360–400°C after

1.5 kh aging is consistent with the theoretical activation energy of spinodal decomposition in which after 1.5 kh of aging, only 400°C would have the needed energy for activation [14].

After 10 kh of aging (not shown), the second peak distance extends only slightly for all materials studied so far – including the EPRI material aged only for 10 kh. The second peak distance after aging at 400°C for CF3M is 7.4nm, for CF3 is 7.4nm, and for CF8 is 6.9nm. Data on the "model" CF8M alloys after 10 kh has not been collected yet. Though for the EPRI alloys have similar characteristics; the second peak distance for CF3 is 6.6nm, for CF8 is 7.2nm, and for CF8M is 7.4nm. Furthermore, 360°C aging after 10 kh approaches the values for 400°C aging after 1500 hours. While the concentration amplitude was shown to continue to rise substantially, the spatial wavelength of the decomposed regions only increased a small amount at 400°C. This points to a conclusion that the driving force for spinodal decomposition begins to reduce after 10 kh at 400°C.
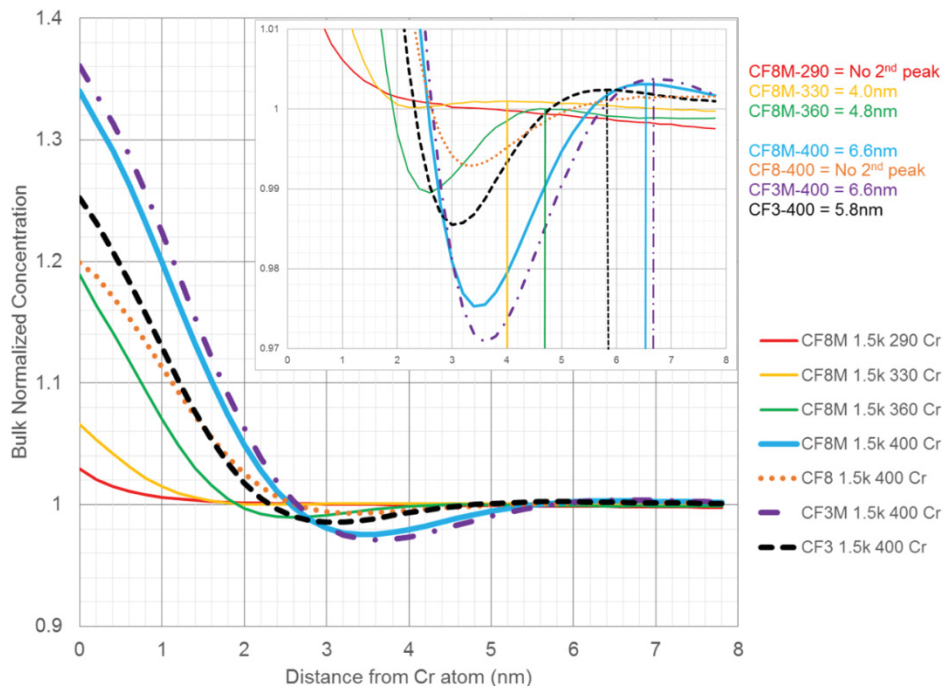
Figure 22. Radial distribution function from Cr of Cr atoms in CF8M alloys aged for 1.5 kh at 290–400°C and CF3 alloy aged for 1.5 kh at 400 °C. Inset: distance to second peak in RDF which is indicative of Cr-rich α` wavelength.

5.3. Quantification of G-phase precipitation within ferrite phase of model CASS alloys

For G-phase precipitation, the Ni RDFs for each model CASS alloy at different aging temperatures after 1.5 kh of aging is shown in Figure 23. Whereas the degree of Cr-segregation was largely dependent on Mo composition, the degree of Ni-segregation is mostly dependent on C composition with some additional dependence on Mo composition. At 400 °C after 1.5 kh aging, the low C CF3 and CF3M alloys have much greater Ni-segregation than the high C CF8 and CF8M alloys, with the Mo bearing alloys, CF3M and CF8M, having larger Ni-segregation

than their respective low-Mo counterparts, in agreement with Pareige et al [25]. The importance of low-C on the kinetics of G-phase formation is agreement with Mburu et al [38], where they found CF3 alloys formed G-phase particles after aging for 4300 hours at 360 and 400°C while CF8 alloys only formed them at 400°C. All four alloys tested in this study did exhibit some G-phase precipitation after only 1.5 kh of aging at 400°C. The 360°C data all had approximately the same amount of Ni-segregation towards Ni atoms at a relatively low bulk normalized concentration; the reason for the large jump in the CF3 alloy from 360°C to 400°C is likely due to, as reported elsewhere [25,38], the nucleation and growth of G-phase particles requires a two-stage process of expulsion Ni from α` and Si from α followed by precipitate nucleation at the α/α`interface. The interaction of C with austenite stabilizers Ni and Mn in the Fe-rich α phase along with a solute drag effect on Mo and repulsive interaction with Si may account for the high C alloys having less G-phase precipitation than the low C alloys [39,40]. After 10 kh aging, the degree of Ni separation increases dramatically, where in three alloys – CF8M, CF8, and CF3 – Ni separation is greater in the material aged at 360°C after 10 kh than the material aged at 400°C after 1.5 kh. The CF3M alloy already had a large Ni separation at 400°C after 1.5 kh. This shows that G-phase precipitation takes place after spinodal decomposition – as it forms heterogeneously on the α` interface – and is highly aging time and aging temperature dependent.
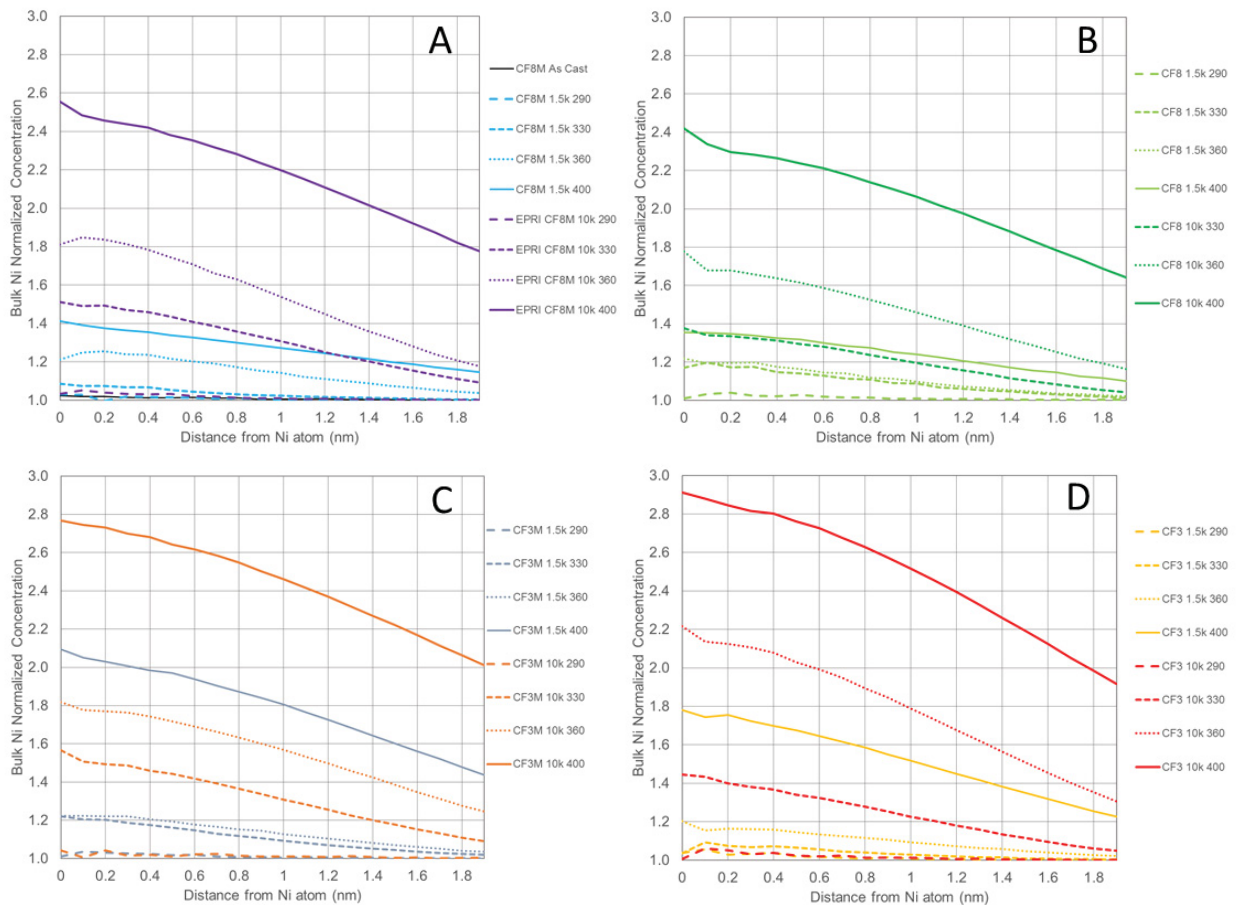

Figure 23. Radial distribution function for Ni Concentration from Ni atoms in (a) CF8M, (b) CF8, (c) CF3M, and (d) CF3 after 1,500 hours and 10,000 hours thermal aging

5.4. Frequency distribution of elements within ferrite phase of model CASS alloys

There are also other ways of quantifying the degree of microstructural evolution inside the ferrite phase of these model CASS alloys using the APT data. One such way is through the use of frequency distribution functions. The frequency distribution functions gather the atoms into 200 ion bins of nearest neighbors, calculates the composition of the bins, and creates a distribution of the compositions among all the bins in the reconstruction. A fully homogeneous alloy should have a normal distribution centered on the bulk concentration of each element; the difference from this normal distribution corresponds to the degree of elemental segregation. Figure 24 shows the frequency distribution functions of Fe, Cr, and Ni of each alloy aged at each temperature after both 1.5 kh and 10 kh. The Fe peak shifts to the right and the Cr and Ni peaks shift the left as Fe is the bulk element and becomes more pure during spinodal decomposition. However, the number of higher than normal Cr and Ni bins also increases with aging. The high Mo alloys clearly have the largest change among the alloys with CF3M experiencing the most change. CF8 undergoes the least amount of change within the ferrite.
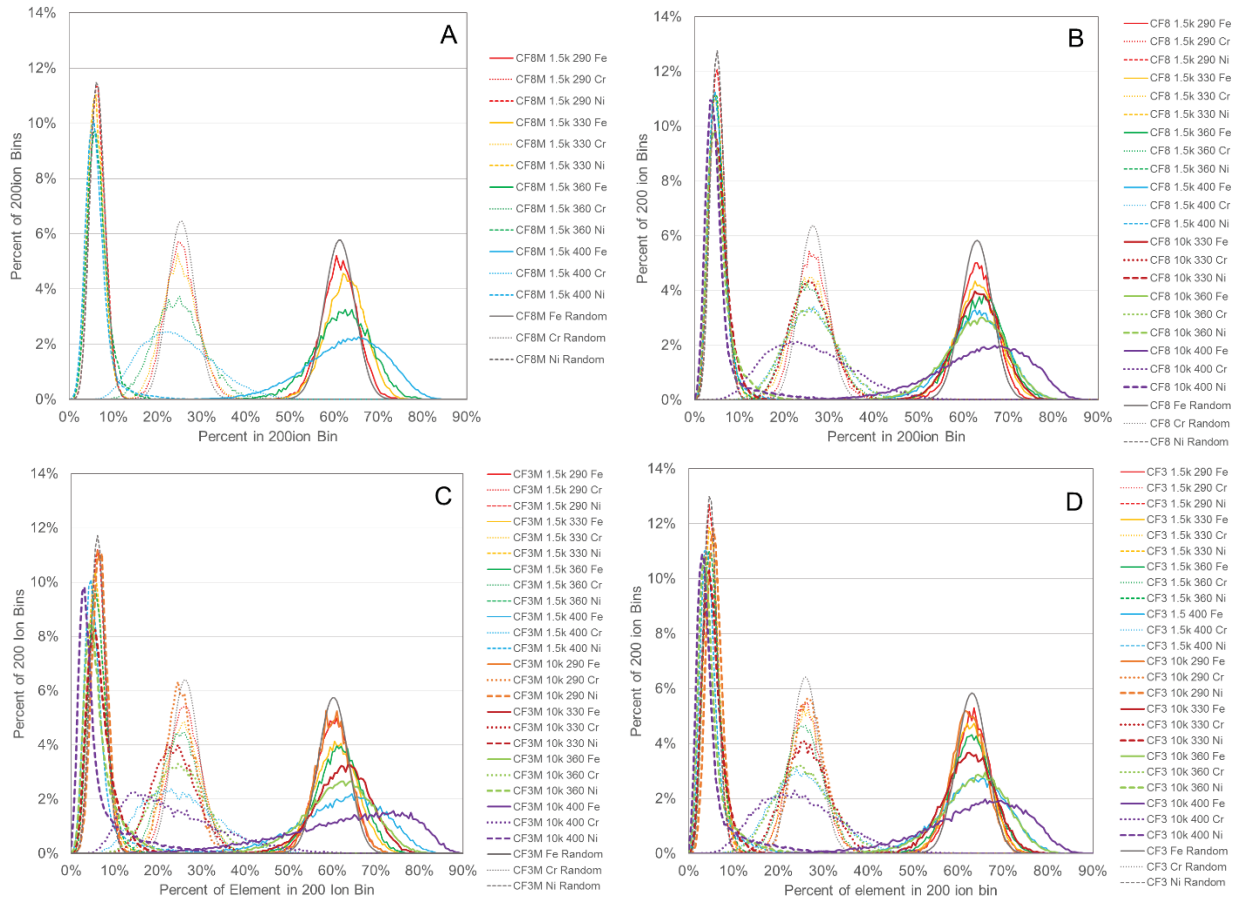

Figure 24: Frequency distribution functions of Fe, Cr, and Ni atoms for (a) CF8M, (b) CF8, (c) CF3M, and (d) CF3 alloys after 1.5 kh and 10 kh aging at all four temperatures

6. MICROSTRUCTURAL EVOLUTION AT AUSTENITE/FERRITE BOUNDARY

6.1. Segregation of solute to the phase boundary in model CASS alloys

While spinodal decomposition and G-phase precipitation take place internally in the ferrite phase, there are also important microstructural and elemental changes occurring on the austenite-ferrite interphase boundary, particularly in the higher C and/ or higher Mo steels. The same effect of the complex interaction of the solute elements with each other, particularly seen in the G-phase precipitation behavior among Mo, Si, Mn, and C, is also seen at the phase boundary. The lower Mo, lower C CF3 steel has the least amount of segregation observed at the phase boundary based on STEM-EDS mapping shown in Figure 25 comparing the as-cast condition to the 330°C and 400°C aging after 1.5 kh. In CF3, as is the case in the other steels as well, Fe and Ni are preferentially in austenite, while Cr and Si are preferentially in the ferrite. Unfortunately in this and the other EDS maps presented here, the Mn and Cu signals were low. As such, the effect of these elements on segregation to the boundary in these materials is presently not known. Further characterization by APT of the phase boundary will be completed in the future.
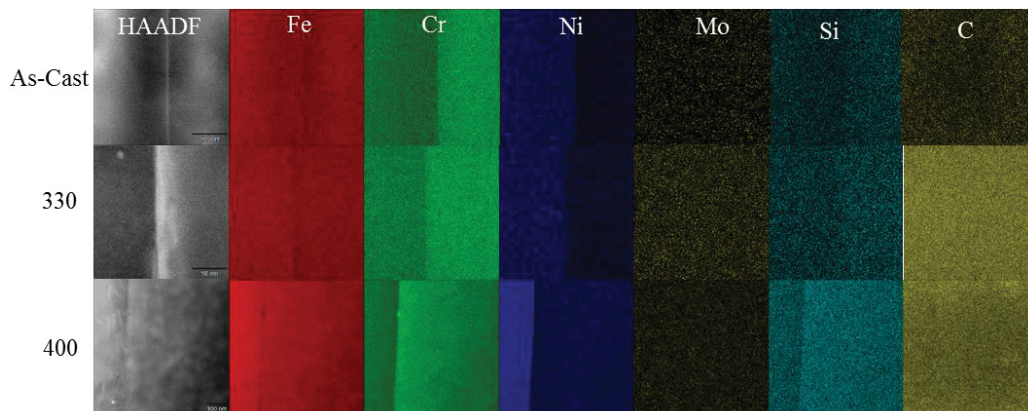

Figure 25: STEM-EDS mapping of segregation at phase boundary in model CF3 alloy in the As-Cast condition and after aging for 1.5 kh at 330°C and 400°C.

Influence by the larger concentration of Mo, segregation to the phase boundary is evident in the CF8M and CF3M alloys, but without formation of carbides, as will be shown later in CF8. As shown in the STEM-EDS maps in Figure 26, Mo and Cr both segregate to the interphase boundary, even in the as-cast condition. After thermal aging, Si and to a smaller extent C also segregate to the interphase boundary. It is clear that the interaction of Mo, Si, Cr, and C at the boundary reduces the tendency to form any carbide phases at the boundary that grow into the austenite. This segregation is also seen in the CF3M alloy but to a lesser extent than in the CF8M alloy, possibly due to the lack of C at the interface prompting less segregation of Mo and Si to the interface and more spinodal decomposition and G-phase precipitation as observed in the previous APT data.
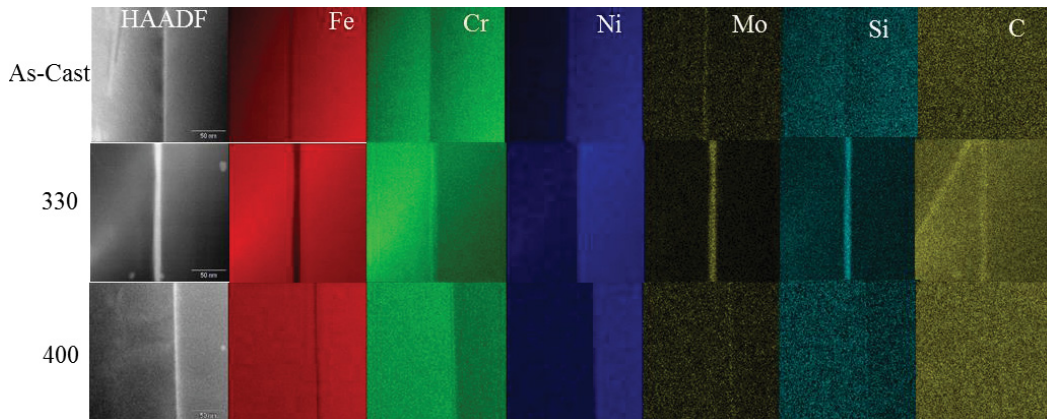
Figure 26: STEM-EDS mapping of segregation at phase boundary in model CF8M alloy in the As-Cast condition and after aging for 1.5 kh at 330°C and 400°C.

6.2. Formation and growth of carbides at phase boundary in model CF8 alloys

The higher C, lower Mo alloy CF8 is similar to the CF3 alloy in that little segregation at the phase boundary between ferrite and austenite is observed, though carbides have formed in many locations on the phase boundary; see Figure 26. These carbides are observed in a limited extent in the as-cast condition but are much more prevalent in the aged materials, both at 330 °C and 400 °C. They tend to be rich in Cr and slightly enriched in Mo with depletion in Fe, Ni, and Si. This is also observed in the EPRI CF8 alloys aged for 10 kh at 330°C, 360°C, and 400°C. Based on the as-cast condition where C is not enriched in the clusters shown, it appears that at least in some cases, the Cr segregates into clusters along the interphase boundary before absorbing C during aging to form a carbide. In the DF TEM image and SAED pattern of a CF8 alloy aged at 330°C for 1.5 kh in Figure 27, it is seen that the Cr-rich carbides, which have the $M_{23}C_6$ structure, form cube-on-cube on the austenite side of the boundary and grow into the ferrite. Further evidence pointing to the carbides growing into the ferrite phase is shown in the STEM-EDS line scans across the Cr-rich regions (carbides in the aged samples) in Figure 28, where there is a depletion of Cr near the carbide in the ferrite but not so in the austenite; the Cr diffuses towards the carbide from the ferrite, thus depleting the surrounding ferrite. This depletion width increases to more than 100 nm after 10 kh aging. This depletion region is approximately 50nm from the carbide/ferrite interface. This growth of Cr-rich carbides at the phase boundary may potentially be the reason that the ferrite phase experiences the least amount of decomposition of the four alloys due to a reduction of available Cr.
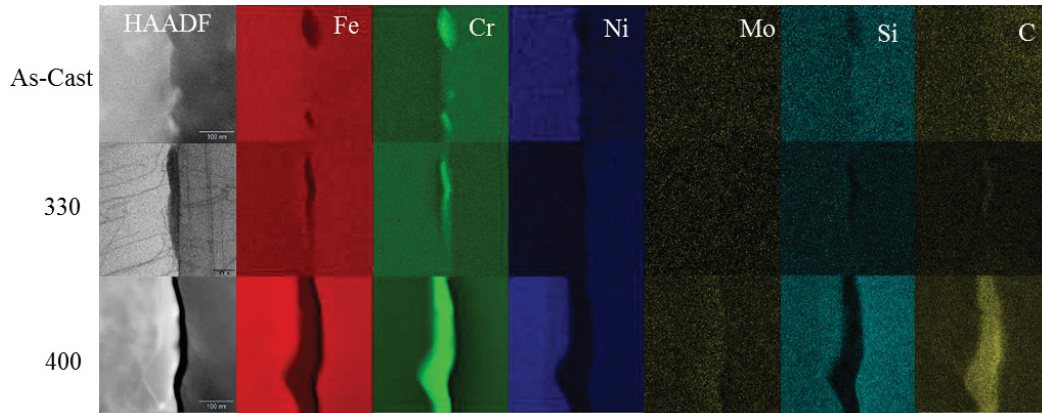
Figure 27. STEM-EDS mapping of segregation and carbide growth at the ferrite (left) and austenite phase boundary in CF8 alloy in the As-Cast condition and after aging for 1.5 kh at 330°C and 400°C.
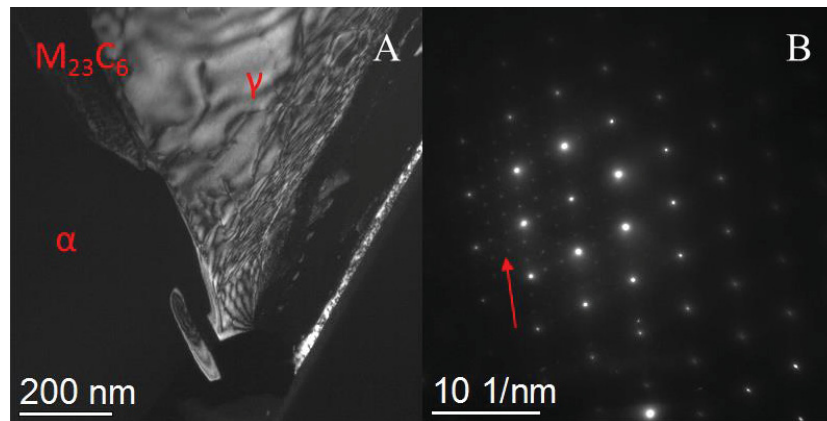
Figure 28. (A) TEM DF image using (011)γ reflection and (B) SAED at (011)γ zone axis of a carbide at the interphase interface in a CF8 alloy aged at 330°C for 1.5 kh. Faint reflections, indicated by red arrow, that are 1/3 the d-spacing of the strong γ reflections are from the $M_{23}C_6$.

Figure 29: STEM-EDS line scan of carbide at phase boundary in CF8 alloy in the As-Cast condition (black) and after aging for 1.5 kh at 330°C (blue) and 400°C (red).
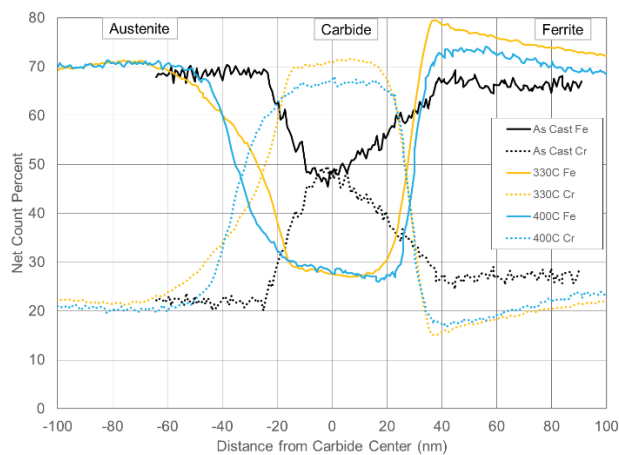
6.3. Decomposition and precipitate denuded zone on ferrite side of phase boundary in EPRI-provided CASS alloys after 10 kh aging

Evidence for future research, primarily by APT and correlative STEM, is presented in Figure 30. These are STEM-BF images of phase boundaries in EPRI-provided CF8M, CF8, and CF3 alloys aged at 400°C for 10 kh. As indicated by the blue arrows, there is evidence for a decomposition and G-phase precipitate denuded zone near the phase boundary on the ferrite side. This is not readily apparent in the alloys aged for 1.5 kh, but is visible in all the alloys aged for 10 kh observed so far. The chemical distribution and composition in this region is an important aspect that will be further investigated in the future.
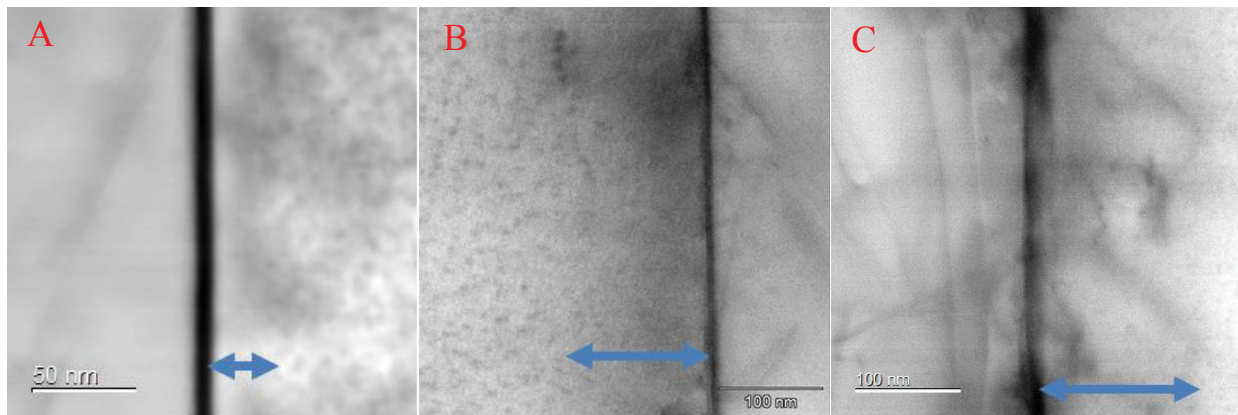

Figure 30. STEM-BF of EPRI alloys aged at 400°C after 10 kh; (a) CF8M, (b) CF8), (c) CF3

7. SUMMARY AND CONCLUSIONS

The CASS portfolio in the project includes four model CASSs (CF3, CF3M, CF8, and CF8M) and four EPRI-provided CASSs (CF3, two CF8s, and CF8M). These materials have been thermally aged at LWR-relevant temperatures (290 and 330°C) and at accelerated-aging temperatures (360 and 400°C) for more than two years as of today. Two wrought stainless steels, 304L and 316L, have also been aged along with the cast stainless steels to obtain reference property degradation data for austenite single phase (not reported here). The key mechanical and microstructural characterizations have been completed for the eight CASS materials aged up to 10000 hours and the results are presented in this report, which are summarized as below:

(1) *Strength and ductility of model alloys:* The strength of the model cast stainless steels with 4–16% initial δ-ferrite content decreased gradually with aging time and the decreased amounts were higher at the relatively lower aging temperatures of 290 and 330°C. The thermal aging treatments had negligible effect on the general temperature dependence of strength in the model alloys: the YS and UTS decreased with test temperature at similar rates below aging temperatures but became nearly temperature independent in the aging temperature range of 290–400°C. The strengths of the Mo-containing (2.3–2.6 wt.%) alloys, CF3M and CF8M, were always higher than those of their counterparts with lower Mo content (<0.5 wt.%), CF3 and CF8.

The model alloys showed reduction of ductility during the short-term 1.5 kh aging but experienced ductilization during aging for 1.5 to 10 kh: both UE and TE significantly decreased after aging for 1.5 kh, and then they partially recovered in further aging to 10 kh. The UE and TE decrease with test temperature before they become nearly temperature independent above ~200°C. Despite significant ductility reductions, the less ductile CF3 and CF3M alloys retained high uniform ductility > ~20% over the whole test temperature range.

(2) *Strength and ductility of EPRI-provided alloys:* In these cast stainless steels with relatively high (11–33%) initial δ-ferrite content, the thermal aging effect is largely muted in the strength parameters. Different processing routes, however, have caused some noticeable differences in aging behavior. The YS of the centrifugal cast alloys (from CF3-piping and CF8M-piping) was lower than those of the static cast alloys (from CF8-piping and CF8-elbow), which is mainly because of the much higher δ-ferrite content in the static cast alloys (in the order of 30% versus of 10%). Despite the varied amounts of δ-ferrite, however, the UTS data show little difference between the centrifugal and static cast alloys.

The UE and TE datasets indicated that these high ferrite CASSs slightly lose their ductility during the 10 kh aging. The biggest and exceptional ductility reduction was observed in the static cast CF8-elbow material with the highest δ-ferrite content of 33%. Despite large data scatters and some aging-induced reductions, the vast majority of UE and TE data remained above ~20% over the whole test temperature range of 25–400°C. Just a few ductility data were slightly below the 20% mark only in the aging temperature range. Both the ductility parameters of this material show little temperature dependence over the whole test temperature range.

(3) *Impact toughness of model alloys:* The molybdenum containing alloys (CF3M and CF8M) showed evident aging temperature dependence while the decrease of USE in CF3 and CF8 was rather sudden in the 1.5 kh aging, and then showed little aging temperature dependence up to 10 kh. The maximum percent reduction of USE measured after aging was limited to <

50% and it was nearly independent of alloy composition as the maximum reductions of USE for all model alloys fall within a narrow range of 43–49%. Overall, the USE data for model alloys showed relatively insignificant aging temperature dependence while the DBTT data exhibited more aging-temperature and alloying element (Mo and C) dependences and complex degradation behavior. The CF3M alloy showed its DBTT shifted above room temperature (+9°C or ΔDBTT = +135°C) after aging at 360°C for 10 kh. The smallest shift (ΔDBTT), +17, was found in the CF8 alloy after aging at 400°C for 10 kh. An aging recovery of DBTT (or negative shift of DBTT) between 1.5 kh and 10 kh was evident in the low temperature (290 and 330 °C) aging.

(4) *Impact toughness of the EPRI-provided alloys:* The molybdenum content can cause the biggest effect on USE before aging but the δ-ferrite content is the biggest factor determining the reduction of USE. The CF8M alloy with 2.51% Mo has the lowest USE before aging but the reduction of USE by aging is larger in the static cast CF8 alloys with 25 and 33% δ-ferrite. The centrifugal cast CF3 (from Z21 pipe ring) showed significant DBTT shifts by aging but thermal recovery (i.e., decrease of DBTT) became apparent after aging at 360 and 400°C. The CF8M alloy (K23, centrifugal cast) also demonstrated the recovery behavior in the 400°C aging after its DBTT increased well above room temperature by the 360°C aging. Overall, the static cast CF8 alloys have much higher δ-ferrite content of 25–33% in average and display correspondingly more significant degradation of impact energy. Both of the static cast materials, CF8 (S43 ring) and CF8 (elbow), displayed a profound and temperature-dependent shift of DBTT after aging. Both the high Mo content and the high δ-ferrite volume fraction are believed to be the prerequisite factors that can induce significant degradation or embrittlement.

(5) *Microstructural changes after aging:* A larger volume fraction of δ-ferrite in the sample, which is affected by the chemistry including the Mo and C concentrations and processing route that determines cooling rate, increased the potential for embrittlement as the ferrite phase and ferrite/austenite phase boundary underwent microstructural changes while the austenite matrix had very limited changes. Increasing Mo content strongly increased the degree of spinodal decomposition with decreasing C slightly acting as a synergistic effect; and similarly, decreasing C had a strong tendency to increase the degree of G-phase precipitation with increasing Mo acting in a synergistic manner.

(6) *Correlation between microstructural and mechanical property changes*: The correlation between degradation of absorbed impact energy from the Charpy tests with the degree of spinodal decomposition and G-phase precipitation is rather strong; the CF8 alloy had the least amount of decomposition and G-phase precipitation and had the least change in impact properties, while the high Mo and low C alloys had the greatest degree of microstructural evolution and the largest reduction in impact properties. Also, Mo and C tend to segregate to the phase boundaries and enhance diffusion towards or away from the boundaries as well, due to the increased attraction/repulsion induced by the Mo and C. These new phases and high solute concentration regions on the phase boundaries likely influence the thermal aging degradation of these materials. This can be inferred as the high Mo alloys, CF3M and CF8M, both have a larger aging temperature dependence on their impact properties. Further characterization by APT of the phase boundaries of the 1.5 kh and 10 kh aged samples will enlighten the phase boundary importance.

REFERENCES

[1] J.T. Busby, P.G. Oberson, C.E. Carpenter, M. Srinivasan, *Expanded Materials Degradation Assessment (EMDA)-Vol. 2: Aging of Core Internals and Piping Systems,* NUREG/CR-7153, Vol. 2, ORNL/TM-2013/532, October 2014.

[2] R. Dyle, *Materials Degradation Matrix and Issue Management Tables Overview-LTO Update* (Presented at the Second Workshop on U.S. Nuclear Power Plant Live Extension, Washington, D.C, 2011).

[3] M. Blair, T.L. Stevens, *Steel Castings Handboo*k, ASM International, 1995.

[4] ASTM A743/A743M-13, *Standard Specification for Castings, Iron-Chromium, Iron-Chromium-Nickel, Corrosion-Resistant, for General Application.*

[5] ASTM A744/A744M-13, *Specification for Castings, Iron-Chromium-Nickel, Corrosion Resistant, for Severe Service.*

[6] ASTM A351/A351M-14, *Standard Specification for Castings, Austenitic, for Pressure-Containing Parts.*

[7] K. Chopra and A. Sather, *Initial Assessment of the Mechanisms and Significance of Low-Temperature Embrittlement of Cast Stainless Steels in LWR Systems (*NUREG/CR–5385, 1990).

[8] K. Chopra, *Effects of Thermal Aging and Neutron Irradiation on Crack Growth Rate and Fracture Toughness of Cast Stainless Steels and Austenitic Stainless Steel Welds* (NUREG/CR-7185, 2014).

[9] K. Chopra, *Estimation of Fracture Toughness of Cast Stainless Steels during Thermal Aging in LWR Systems* (NUREG/CR-4513, 1991).

[10] W.F. Michaud, P.T. Toben, W.K. Soppet, and O.K. Chopra, *Tensile-Property Characterization of Thermally Aged Cast Stainless Steels (*NUREG/CR-6142, 1994).

[11] H.M. Chung and T R. Leax, *Mater. Sci. Technol.* 6, 249–262 (1990).

[12] H.M. Chung, *Evaluation of Aging of Cast Stainless Steel Components* (Presented at ASME Pressure Vessel & Piping Conference, San Diego, CA, 1991).

[13] H.M. Chung, *Presented at the American Society for Mechanical Engineers-Material Properties Council Symposium on Plant Life Extension for Nuclear Components* (Honolulu, Hawaii, 1989).

[14] T.S. Byun, J.T. Busby, *Cast Stainless Steel Aging Research Plan,* ORNL/LTR-2012/440, September 2012.

[15] T.S. Byun, Y. Yang, N.R. Overman, J.T. Busby, *Thermal Aging Phenomena in Cast Duplex Stainless Steels,* JOM, 68(2) (2016) 507-526.

[16] S. Li, Y.L. Wang, H.L. Zhang, S.X. Li, K. Zheng, F. Xue, X.T. Wang, *J Nucl. Mater.* 433, 41 (2013).

[17] M. Murayama, Y. Katayama and K. Hono, *Metall. Mater. Trans. A.* 30A, 345 (1999).

[18] T. Sourmail, *Mater. Sci. Tech.* 17, 1 (2001).

[19] L.P. Stoter, *J. Mater. Sci.* 16, 1039 (1981).

[20] B. Weiss and R. Stickler, *Metal Trans.* 3, 851 (1972).

[21] J.E. Spruiell, J.A. Scott, C.S. Ary, and R.L. Hardin, *Metal Trans.* 4, 1533 (1973).

[22] J. Charles *Proceedings of Duplex Stainless Steel Conference*, Vol 1 (Les Editions de Physique, Les Ulis Cedex, 1991) pp. 3-48.

[23] K.H. Lo, C.H. Shek, J.K.L. Lai, *Mater Sci Eng. R* 65, 39 (2009).

[24] P. Hedström, S. Baghsheikhi, P. Liu, J. Odqvist, *Mater. Sci. Eng. A* 534, 552 (2012).

[25] C. Pareige, S. Novy, S. Saillet, P. Pareige, *J. Nucl. Mater.* 411, 90 (2011).

[26] T.S. Byun and I.S. Kim, *J Mater. Sci.* 26, 3917 (1991).

[27] T.S. Byun and I.S. Kim, *J Mater. Sci.* 28, 2923 (1993).

[28] W. Oldfield, *Curve Fitting Impact Test Data: A Statistical Procedure, ASTM Standardization News,* 3(1 1) (1975) 24-29.

[29] K. Yeager, *Nonlinear curve fitting and the Charpy impact test: statistical, mathematical, and physical considerations* (https://www.uakron.edu/dotAsset/2116623.pdf).

[30] S.K. Kim, Y.S. Kim, *Estimation of Aging Embrittlement of LWR Primary Pressure Boundary Components,* J. Kor. Nucl. Soc. 30(6) (1998) 609-616.

[31] T.S. Byun, N.R. Overman, T.G. Lach, Mechanical Properties of Model Cast Austenitic Stainless Steels after Thermal Aging for 1500 Hours, M2LW-16OR0402152 (PNNL-25377), April 2016.

[32] B. Myers, TEM Sample Preparation with the FIB/SEM. NUANCE Center. Northwestern University, 2009.

[33] A. Devaraj, D.E. Perea, J. Liu, L.M. Gordon, T.J. Prosa, P. Parikh, D.R. Diercks, S. Meher, R.P. Kolli, Y.S. Meng, S. Thevuthasan, *Three-Dimensional Nanoscale Characterization of Materials by Atom Probe Tomography,* International Materials Review (2017) 1.

[34] T.S. Byun, *Acta Materialia,* 51 (2003) 3063–3071.

[35] T.S. Byun, N. Hashimoto, K. Farrell, Acta Materialia, 52 (2004) 3889–3899.

[36] J.Talonen, H.Hänninen, *Formation of shear bands and strain-induced martensite during plastic deformation of metastable austenitic stainless steels,* Acta Materialia, 55 (2007) 6108-6118.

[37] J. Zhou, et al. *Quantitative Evaluation of Spinodal Decomposition in Fe-Cr by Atom Probe Tomography and Radial Distribution Function Analysis*, Microscopy and Microanalysis, 19 (2013) 665-675.

[38] S. Mburu, R.P. Kolli, D.E. Perea, S. Ankem, *Effect of Aging Temperature on Phase Decomposition and Mechanical Properties in Cast Duplex Stainless Steels*, Materials Science and Engineering A 690 (2017) 365-377.

[39] M. Hillert, L. Hoglund, and J. Agren, *Role of Carbon and Alloying Elements in the Formation of Bainitic Ferrite.* Metallurgical and Materials Transactions A, 35A (2004) 3693-3700.

[40] H.P. Van Landeghem, B. Langelier, D. Panahi, G.R. Purdy, C.R. Hutchinson, G.A. Botton, and H.S. Zurob, *Solute Segregation during Ferrite Growth: Solute/Interphase and Substitutional/Interstitial Interactions*, Journal of Materials, 68 (2016) 1329-1334.

(END OF REPORT)